

Supporting Information

Improving the Potential of ParaCEST through Magnetic-coupling Induced Line Sharpening

Xin Guo,^a Lei Zhang,^{bc} Jiesheng Hu,^a Balázs Szilágyi,^{de} Meng Yu,^{*a} Shizhen Chen,^{*bc} Gyula Tircsó,^d
Xin Zhou,^{bc} Jun Tao^{*a}

^aKey Laboratory of Cluster Science of Ministry of Education, School of Chemistry and Chemical Engineering, Liangxiang Campus, Beijing Institute of Technology, Beijing 102488 (China). E-mail: mengyu@bit.edu.cn, taojun@bit.edu.cn

^bAddress State Key Laboratory of Magnetic Resonance and Atomic and Molecular Physics, National Center for Magnetic Resonance in Wuhan, Wuhan Institute of Physics and Mathematics, Innovation Academy for Precision Measurement Science and Technology, Chinese Academy of Sciences—Wuhan National Laboratory for Optoelectronics, Wuhan 430071 (China). E-mail: chenshizhen@wipm.ac.cn

^cUniversity of Chinese Academy of Sciences, Beijing 100049 (China)

^dDepartment of Physical Chemistry, Faculty of Science and Technology, University of Debrecen, Egyetem tér 1, H-4032 Debrecen (Hungary)

^eDoctoral School of Chemistry, University of Debrecen, Egyetem tér 1, H-4032 Debrecen (Hungary)

Supporting Information

Contents

1. Materials and Methods.	4
2. Synthetic Methods	5
3. Computational Details	6
4. Additional Tables.....	7
Table S1. X-ray crystallography data for 1 , 1' and 2	7
Table S2. Selected bond lengths (Å) and bond angles (°) for 1 , 1' and 2	8
Table S3. Distortion parameters for 1 , 1' and 2	9
Table S4. CShM analysis data for 1 , 1' and 2	9
Table S5. Comparison of % CEST of the Ni(II) analogues.	10
5. Additional Figures	12
Fig. S1 The phenolato-ring and the Ni ₂ O ₂ plane of 1 form a dihedral angle of 17.47°. ...	12
Fig. S2 ORTEP plot of 1'	12
Fig. S3 Overlay of crystal structures for 1 and 1'	13
Fig. S4 The phenolato-ring and the Ni ₂ O ₂ plane of 1' form a dihedral angle of 17.35°. ...	13
Fig. S5 The phenolato-rings of 2 form a dihedral angle of 23.48°.....	14
Fig. S6 Electrostatic potential (ESP) map of 1 and 2	14
Fig. S7 UV-vis spectra of 0.10 mM of L in MeOH	15
Fig. S8 UV-vis spectra of a solution containing 0.10 mM (left) and 5.0 mM (right) of 1 in 50 mM HEPES and 100 mM NaCl at pH 7.2.	15
Fig. S9 UV-vis spectrum of a solution containing 0.10 mM of 2 in 50 mM HEPES and 100 mM NaCl at pH 7.2.....	16
Fig. S10 UV-vis spectra of a solution containing 0.10 mM of 1 after the addition of 5 mM CaCl ₂	16
Fig. S11 UV-vis spectra of a solution containing 0.10 mM of 1 after the addition of 4 mM ZnCl ₂	17
Fig. S12 UV-vis spectra of a solution containing 0.10 mM of 1 after the addition of 4 mM Na ₂ CO ₃ and NaH ₂ PO ₄	17
Table S6. Protonation and stability constants of ligand and Ni(II) complex (I = 0.15 M NaCl and T = 25 °C).....	18
Fig. S13 pH-potentiometric titration curve of 1.96 mM ligand in the absence (black dots) and in the presence of one (blue) and two equivalents (red) of NiCl ₂ (I=0.15 M NaCl, T=25 °C).	19
Fig. S14 Spectral changes observed upon titrating of 0.16 mM ligand with NaOH (I=0.15 M NaCl, T=25 °C).	19
Fig. S15 Magnetization and reduced magnetization curves of 1 at the respective temperatures	20
Fig. S16 Variable-pH magnetic susceptibility data for 1 in aqueous solutions containing 50 mM HEPES and 100 mM NaCl at 25 °C.....	21
Table S7. Peak positions, T ₁ Values, distances of hydrogens to Ni, and tentative assignments for 1 recorded under 500 MHz at 37 °C.	21
Fig. S17 500 MHz ¹ H NMR spectrum of 1 in D ₂ O at 310 K.....	22

Fig. S18 500 MHz ^1H NMR spectra of 1 in D_2O at 298 K (navy) and 310 K (maroon) ..	22
Fig. S19 400 MHz ^1H NMR spectrum of 1 in D_2O (red) and 50 mM HEPES and 100 mM NaCl at pH 7.2 (blue).	23
Fig. S20 CEST spectrum recorded at 9.4 T of 10 mM 1 in 50 mM HEPES buffer solution at pH 7.15 and 37 °C, with a 4 s presaturation pulse of 24 μT	23
Fig. S21 CEST spectra recorded at 9.4 T of 10 mM 1 in 50 mM HEPES buffer solution at pH 7.15 and 37 °C	24
Fig. S22 CEST spectra recorded at 9.4 T of 10 mM 1 in 50 mM HEPES buffer solution at pH 7.40 and 37 °C.	25
Fig. S23 Omega plot of 10 mM 1 in 50 mM HEPES buffer solution at pH 7.15 and 37 °C	26
Fig. S24 Omega plot of 10 mM 1 in 50 mM HEPES buffer solution at pH 7.40 and 37 °C	26
Fig. S25 400 MHz ^1H NMR spectrum of 2 in D_2O	27
Fig. S26 Plots of $(1/T_1)$ versus concentration of 1	27
Fig. S27. Plots of $(1/T_1)$ versus concentration of 2	28
Fig. S28 400 MHz ^1H NMR spectrum of C3-N in CD_3OD	28
Fig. S29 400 MHz ^1H NMR spectrum of L in CD_3OD	29
Fig. S30. 100 MHz ^{13}C NMR spectrum of L in DMSO-d_6	29
Fig. S31 IR spectra of solid state samples of L (top), 1 (middle), and 2 (bottom).	30
Fig. S32 Mass spectrum (ESI) for L in MeOH.....	30
Fig. S33 Mass spectrum (ESI) for 1 in MeOH..	31
Fig. S34 Mass spectrum (ESI) for 2 in MeOH.	31
6. References.....	32

1. Materials and Methods.

All reagents and deuterated solvents were used as purchased without further purification. All ^1H and ^{13}C NMR data were recorded on a 400 MHz Bruker AVANCE spectrometer at 298 K. Relaxation time measurements were conducted on a Bruker Advance 500 MHz spectrometer. CEST measurements were conducted on a 400 MHz Bruker 400 WB superconducting NMR spectrometer. Fourier transform infrared (FT-IR) spectra were recorded on a Bruker ALPHA FT-IR spectrometer in the range of 400-4000 cm^{-1} . UV-vis absorption spectra were taken on a Shimadzu UV-1900 spectrometer. High resolution mass spectrometry (HR-MS) data were obtained on an Agilent (Q-TOF 6520) mass spectrometer. The C, H, O and N microanalyses were measured on an Elementar Unicube analyzer.

Magnetic Susceptibility Measurements

Magnetic susceptibility measurements were performed on a Quantum Design MPMS XL7 magnetometer. Powdered samples of **1** were loaded into gelatin capsules and inserted into straws for SQUID analysis. Variable-temperature magnetic susceptibilities were measured from 2 to 300 K at 5000 *Oe*. Variable-field magnetic susceptibilities were measured at 3, 5, 7, 10 K for applied fields ranging from 0 to 7 T.

Solution Magnetic Susceptibility Measurements

The effective magnetic moment was determined based on Evans' method.¹ A degassed solution of 5–10 mM metal complex in D_2O , containing 5% tert-butanol by volume was placed in an NMR coaxial tube with 5% tert-butanol (v/v) in D_2O as reference. The effective magnetic moment (μ_{eff}) was calculated at 298 K by using the equations given below.

$$\chi_g = \frac{3\Delta f}{4\pi f m} + \chi_0 + \frac{\chi_0(d_0 - d_s)}{m} \quad (\text{eq. S1})$$

$$\mu_{\text{eff}} = 2.84\sqrt{\chi_M T} \quad (\text{eq. S2})$$

Δf stands for the proton chemical shift of *tert*-butanol in frequency (Hz) between the reference and paramagnetic sample, the spectrometer frequency (f) in Hz, the mass of the substance per mL of the solution (m), and the mass susceptibility of deuterium oxide ($\chi_0 = -0.6466 \times 10^{-6} \text{ cm}^3/\text{g}$), the density of solvent (d_0) in $\text{g}\cdot\text{cm}^{-3}$, and the density of solvent (d_s) in $\text{g}\cdot\text{cm}^{-3}$. The last term in eq. S2 is neglected. The molar susceptibility (χ_m) is the product of χ_g times the molecular weight of metal complex.² The experiment was repeated two times and averaged.

Relaxation Time Measurements and paraCEST Experiments

All paraCEST spectra were recorded on a 400 MHz Bruker 400 WB superconducting NMR spectrometer (9.4 T) at 37 °C. 10 mM sample of **1** and 30 mM sample of **2** in aqueous buffer solutions containing 50 mM HEPES and 100 mM NaCl were measured and D_2O was placed in an inner capillary to lock the samples. paraCEST spectra were obtained according to the following protocol: ^1H NMR spectra of sample **1** were acquired from -40 to 100 ppm with a step increase of 1 ppm with a 4 s presaturation pulse from 10 to 24 μT at pH 7.15 or 7.40. ^1H NMR spectra of sample **2** were acquired from -40 to 100 ppm with a step increase of 1 ppm at

a power level of $24 \mu T$ at pH 7.40. The paraCEST spectra were plotted by the normalized integrations of the water 1H NMR signal (M_z/M_0) against frequency offset ranging from 100 to -40 ppm referenced to the bulk water signal at 0 ppm to generate a Z-spectrum (CEST spectra). The calculation of exchange rate constants were calculated based on a reported method.³

X-ray Crystallographic Analyses

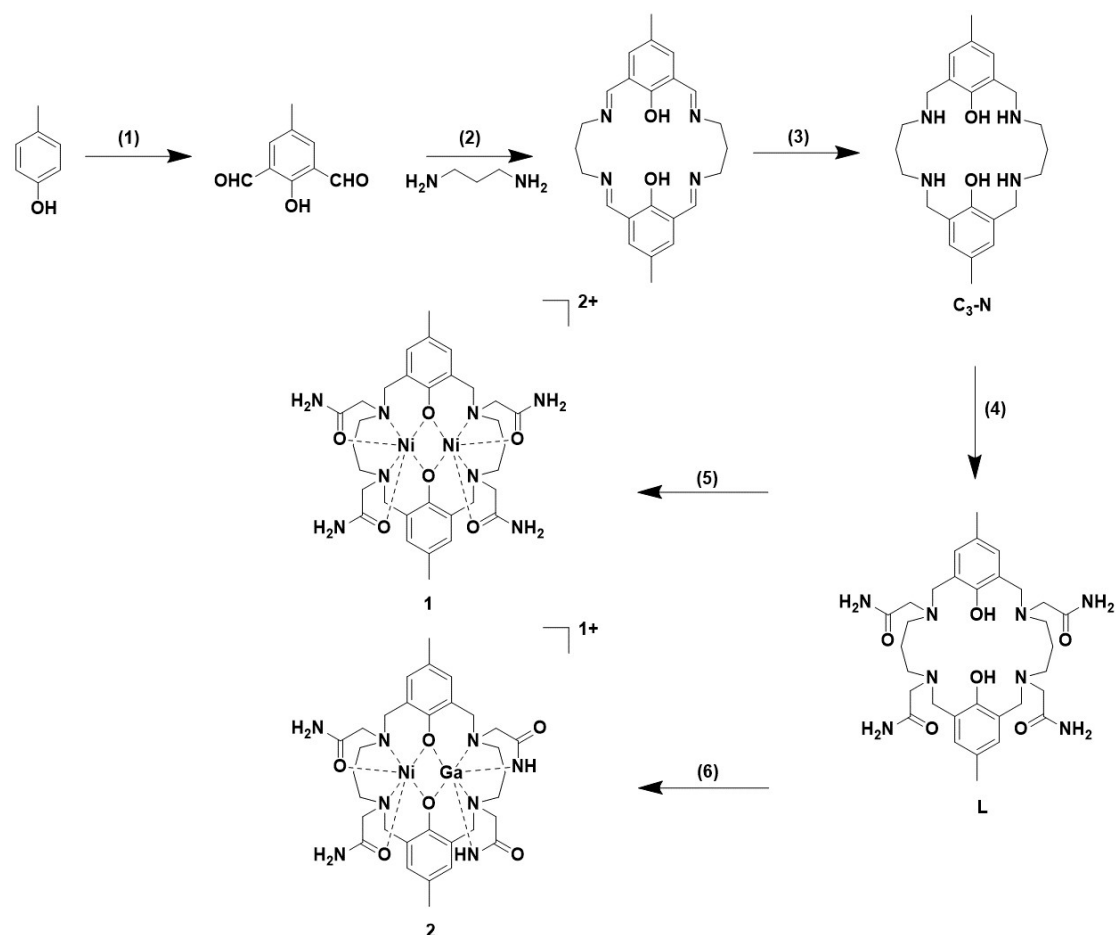
Single-crystal X-ray diffraction data were recorded on a Rigaku Oxford XtaLAB PRO diffractometer with graphite-monochromated Mo $K\alpha$ radiation ($\lambda = 0.71073 \text{ \AA}$). The structures were solved by direct methods and further refined by full-matrix least-squares techniques on F^2 with SHELX program.⁴ The hydrogen atom positions were fixed geometrically at calculated distances and allowed to ride on the parent atoms. Attempts to define the highly disordered solvent molecules were unsuccessful, so the structure was refined with the PLATON “SQUEEZE” procedure.⁵ Crystallographic data have been deposited with the CCDC no. 2291721-2291723.

pH-potentiometric Titration

The aqueous speciation of **L** and its Ni(II) complex was assessed by using pH-potentiometry and UV-vis spectrophotometry. pH-potentiometric titrations were performed with Metrohm 888 Titrando equipped with a jacketed, airtight glass titration vessel and Metrohm 6.0234.100 combined electrode in the pH range of 1.75–11.85. The pH meter was calibrated before each titration using KH-phthalate (pH=4.005) and borax (pH=9.177) buffer solutions prepared from commercial buffers. The H^+ concentrations were calculated from the measured pH values by applying the method proposed by Irving et al.⁶ A solution of approximately 0.01 M HCl was titrated with a 0.15 M NaOH solution (0.15 M NaCl), and the differences between the measured and calculated pH values (for the points with $pH < 2.2$) were used to calculate the $[H^+]$ from the pH values measured in the titration experiments. The measured points with $pH > 11.0$ of the acid-base titration were used to calculate the ionic product of water (pK_w) which was found to be 13.913 (0.15 M NaCl) under our experimental conditions. All samples were purged with N_2 prior to analysis and subsequently analyzed under an N_2 atmosphere at 25 °C to prevent CO_2 contamination. The concentration of the ligand was determined based on the pH-potentiometric titration curve obtained in the absence of Ni(II) and it was also confirmed by UV-vis titration using Cu(II) at $pH = 4.80$ buffered by *N,N'*-dimethyl-piperazine buffer ($c_{DMP} = 100 \text{ mM}$). The titrations investigating metal/ligand speciation were performed with 5.00 mL solutions that contained a 1:0 (titration of the ligand only) 1:1 or 1:2 molar mixture of the ligand and $NiCl_2$ (concentration of the ligand in the samples was set to 1.99 mM) Carbonate-free solutions of 0.1684 M NaOH and 0.1932 M HCl were prepared using N_2 -saturated deionized Millipore water. Owing to the solubility problems evidenced during the ligand titration under basic conditions ($pH > 8.0$) the protonation constant of the ligand was also studied at 25 °C and 0.15 M NaCl ionic strength by using JASCO V-750 UV-vis spectrophotometer and quartz cuvettes ($l = 1.0 \text{ cm}$) by recording the spectra of the ligand ($c_L = 0.164 \text{ mM}$) in the wavelength range of 200–400 nm. Protonation constants were calculated with the use of absorbance data recorded at 240, 245, 250, 255, 280, 295, 300, 305, 310, 315, 320 and 325 nm. The molar absorption coefficients of the H_2L form of the ligand were determined in a separate experiment, while

those of the HL and L forms were refined during the data fitting. The PSEQUAD program was used for pH and UV-vis fittings.⁷

2. Synthetic Methods



Scheme S1. Synthesis of L. Conditions: (1) hexamethylenetetramine, TFA, 130 °C, 16h (48%); (2) NaClO₄, acetic acid, EtOH, 75 °C, 3 h (97%); (3) NaBH₄, MeOH, r.t., 3 h (51%); (4) DIPEA, MeCN (anhy.), 70 °C, 48h (71%); (5) Ni(OAc)₂·4H₂O, MeOH, 70 °C, 48 h (34%); (6) (a) Ga(NO₃)₃·xH₂O, MeONa, MeOH, 70 °C, 48 h, (b) Ni(OAc)₂·4H₂O, MeOH, 40 °C, 5 h (62%).

Synthesis of L

The compound C₃-N was synthesized following a modified literature procedure.⁸ ¹H NMR (400 MHz, MeOH-d₄) δ 6.85 (s, 4H), 3.68 (s, 8H), 3.31 (d, *J* = 10.5 Hz, 8H), 2.54 (s, 8H), 2.19 (s, 6H), 1.68 (s, 4H). The NMR data are consistent with those reported in the literature.

The compound L was synthesized following a modified literature procedure.⁹ C₃-N (64 mg, 156 μmol) and DIPEA (163 μL, 936 μmol) were dissolved in 20 mL dry acetonitrile and heated to 60 °C. 2-Bromoacetamide (129 mg, 936 μmol) was then added and the mixture was reacted at 70 °C for 48 h under N₂. Acetonitrile was then removed under vacuum and the crude was purified by reverse phase chromatography using H₂O/MeCN (0.1% HCOOH) as eluent. Product eluted at 30% acetonitrile content and fractions were combined and lyophilized to yield

~71 mg product as a white powder (71%). ¹H NMR (400 MHz, MeOH-d₄) δ 6.85 (s, 1H), 3.68 (s, 2H), 3.30 (s, 1H), 2.54 (s, 3H), 2.19 (s, 2H), 1.68 (s, 1H). ¹³C NMR (101 MHz, DMSO-d₆) δ 182.41, 173.09, 162.78, 139.30, 135.68, 132.59, 66.07, 64.82, 59.17, 29.60. HRMS (ESI⁺): Calcd for (M+H)⁺ (C₃₂H₄₉N₈O₆) 641.3775, found 641.3746. UV-vis absorption spectrum: 288 nm ($\epsilon = 4728 M^{-1}cm^{-1}$). FT-IR (ATR, cm⁻¹): 3290(m); 3170 (m); 2919 (m); 2810 (m); 1683 (s); 1483 (s); 1590(m); 1485 (m); 1456 (m); 1335 (s); 1263 (s); 1232 (w); 1168 (s); 1135 (s); 1049 (s); 999 (m); 882 (m); 581 (s) (see Fig. S31).

Synthesis of 1

L (100 mg, 156 mmol) and Ni(OAc)₂·4H₂O (81.6 mg, 343 mmol) were combined in a 50 mL round bottom flask and dissolved with 15 mL anhydrous MeOH to give a light green solution. After stirring for 48 h at 70 °C, The solution was removed under vacuum and purified by reverse phase to obtain product as blue powder following the lyophilization (80 mg, 59%). (50 mM NH₄OAc solution, pH ~ 6.2 and MeCN containing 5% 50 mM NH₄OAc solution, 20% gradient). Crystals suitable for test were grown from the slow diffusion of isopropyl ether into a saturated MeOH solution of complex 1. HRMS (ESI⁺): Calcd for (M+H)⁺ (C₃₂H₄₅N₈Ni₂O₆) 753.2169, found 753.2177. Anal. Calcd. for C₃₆H₆₃N₈Ni₂O₁₆: C, 44.02; H, 6.57; O, 26.06; N, 11.41%. Found: C, 43.99; H, 6.61; O, 25.03; N, 11.50%. UV-vis absorption spectrum: 305 nm ($\epsilon = 7197 M^{-1}cm^{-1}$), 380 nm ($\epsilon = 105 M^{-1}cm^{-1}$), 590 nm ($\epsilon = 41.3 M^{-1}cm^{-1}$). FT-IR (ATR, cm⁻¹): 1636(s); 1541 (s); 1471 (s); 1397 (s); 1255 (s); 1166 (w); 1028 (m); 970 (s); 863 (m); 803 (m); 589 (s); 490 (m) (see Fig. S31).

Synthesis of 2

L (100 mg, 156 mmol) and Ga(NO₃)₃·xH₂O (39.9 mg, 156 mmol) were combined in a 50 mL round bottom flask and dissolved with 15 mL anhydrous MeOH to give a colorless solution. Sodium methanolate (225 mg, 936 mmol) was then added and the mixture was reacted at 70 °C for 48 h. Ni(OAc)₂·4H₂O (38.8 mg, 156 mmol) was added to the above solution dropwise and stirred for 5 h at 40 °C. The solution was removed under vacuum and purified by reverse phase to obtain product as light green powder after lyophilizing (80 mg, 62%). (50 mM NH₄OAc solution, pH~6.2 and MeCN containing 5% 50 mM NH₄OAc solution, 20% gradient). HRMS (ESI⁺): Calcd for (M+H)⁺ (C₃₂H₄₄GaN₈NiO₆) 765.1976, found 765.1827. Anal. Calcd. for C₃₆H₆₆GaN₈NiO₁₈: C, 42.09; H, 6.48; O, 28.03; N, 10.91%. Found: C, 42.33; H, 6.17; O, 26.58; N, 10.77%. UV-vis absorption spectrum: 295nm ($\epsilon = 5578 M^{-1}cm^{-1}$). FT-IR (ATR, cm⁻¹): 1671(w);1652(m); 1559 (s); 1473 (s); 1397 (s); 1252 (s); 1150 (w); 953 (s); 863 (m); 801 (s); 725; 649 (s); 583 (s); 503 (m); 443(s) (see Fig. S31).

3. Computational Details

Density functional theory (DFT) calculations were performed using the ORCA quantum chemistry software version 5.0.3 and the B3LYP functional.¹⁰⁻¹² Coordinates from crystal structure were directly utilized without further optimization. Def2-TZVPP basis set was used for Ni and all coordinated atoms and def2-TZVP basis set was used for the remaining atoms. The RIJCOSX approximations combined with appropriate Ahlrichs auxiliary basis sets were routinely employed to speed up the calculations.¹³⁻¹⁵ Tight SCF convergence criteria were used

for all calculations. The magnetic exchange coupling constants (J) was calculated using the Yamaguchi formalism according to the following equation where the spin Hamiltonian $\hat{H} = -2J\hat{S}_1\cdot\hat{S}_2$ is assumed.

$$J(1) = -(E_{\text{HS}} - E_{\text{BS}})/S_{\text{max}}^2 (-18.26 \text{ cm}^{-1})^{16,17}$$

$$J(2) = -(E_{\text{HS}} - E_{\text{BS}})/S_{\text{max}}(S_{\text{max}} + 1) (-12.17 \text{ cm}^{-1})^{11}$$

$$J(3) = -(E_{\text{HS}} - E_{\text{BS}})/(\langle S^2 \rangle_{\text{HS}} - \langle S^2 \rangle_{\text{BS}}) (-18.22 \text{ cm}^{-1})^{18}$$

E_{HS} and E_{BS} stand for the energies of the high-spin state ($S = 2$) and broken-symmetry state ($S = 0$) of the dinuclear nickel complex. The broken-symmetry state corresponds to configuration where two unpaired spin-up, α electrons are localized on one site and two unpaired spin-down, β electrons localized on the other site. $\langle S^2 \rangle_{\text{HS}}$ and $\langle S^2 \rangle_{\text{BS}}$ denote the expectation values of the total spin operators for the ferromagnetic and antiferromagnetic spin states, respectively. S_{max} stands for the total spin number of high-spin state.

4. Additional Tables

Table S1. X-ray crystallography data for 1, 1' and 2.

	1	1'	2
CCDC number	2291722	2291721	2291723
Empirical formula	$\text{C}_{38}\text{H}_{62}\text{N}_8\text{Ni}_2\text{O}_{13}$	$\text{C}_{32}\text{H}_{52}\text{Cl}_2\text{N}_8\text{Ni}_2\text{O}_9$	$\text{C}_{33}\text{H}_{48}\text{BrGaN}_8\text{NiO}_7$
Formula weight	956.37	881.13	877.10
Temperature (K)	100.15	293(2)	100.0
Crystal system	monoclinic	monoclinic	monoclinic
Space group	$C2/c$	$P2_1/n$	$C2/c$
a (Å)	15.3815(5)	10.2398(4)	29.4737(12)
b (Å)	18.3733(4)	15.3856(6)	14.7532(5)
c (Å)	16.7250(5)	12.1399(4)	20.5922(8)
α (°)	90	90	90
β (°)	111.493(3)	102.111(3)	103.741(4)
γ (°)	90	90	90
V (Å ³)	4398.0(2)	1870.02(12)	8697.9(6)
Z	4	2	8
ρ_{calcd} (g/cm ³)	1.444	1.565	1.325
μ (mm ⁻¹)	0.927	1.213	1.840
F (000)	2024.0	924.0	3586.0
θ_{max} (deg)	30.0230	28.5660	29.4240
completeness (%)	99.7	99.7	99.7
no. of. rflns collected	28956	25225	58238
no. of. Indep rflns	5711	4760	11178
Goodness of fit on F^2	1.061	1.055	1.021
Final R indexes [$I \gg 2\sigma$ (I)]	$R_1 = 0.0350,$ $wR_2 = 0.0865$	$R_1 = 0.0564,$ $wR_2 = 0.1629$	$R_1 = 0.0462,$ $wR_2 = 0.1180$
Final R indexes [all data]	$R_1 = 0.0380,$ ^a $wR_2 = 0.0882$ ^b	$R_1 = 0.0695,$ $wR_2 = 0.1715$	$R_1 = 0.0646,$ $wR_2 = 0.1254$

$${}^aR1 = \Sigma||F0| - |FC||/\Sigma|F0|. \quad {}^bWR2 = [\Sigma w(F_0^2 - F_c^2)^2/\Sigma w(F_0^2)^2]^{1/2}.$$

Table S2. Selected bond lengths (Å) and bond angles (°) for 1, 1' and 2.

1		1'	
Ni1–O1	2.0119(11)	Ni1–O1	2.026(2)
Ni1–O1¹	2.0159(11)	Ni1–O1¹	2.022(2)
Ni1–O2	2.1184(11)	Ni1–O2	2.070(2)
Ni1–O3¹	2.1109(12)	Ni1–O3	2.080(2)
Ni1–N2¹	2.0885(16)	Ni1–N2	2.092(3)
Ni1–N1	2.0872(15)	Ni1–N1	2.103(3)
O1–Ni1–O1¹	82.80(5)	O1¹–Ni1–O1	83.44(9)
O1–Ni1–O2	95.44(5)	O1–Ni1–O2	90.31(9)
O1¹–Ni1–O2	89.68(4)	O1¹–Ni1–O2	91.78(9)
O1¹–Ni1–O3¹	96.88(5)	O1¹–Ni1–O3	90.32(9)
O1–Ni1–O3¹	91.98(5)	O1–Ni1–O3	92.89(9)
O1–Ni1–N1	88.05(6)	O1–Ni1–N1	87.83(9)
O1¹–Ni1–N1	165.92(6)	O1¹–Ni1–N1	167.29(10)
O1–Ni1–N2¹	167.35(6)	O1–Ni1–N2	166.61(10)
O1¹–Ni1–N2¹	88.09(6)	O1¹–Ni1–N2	87.11(9)
O3¹–Ni1–O2	170.66(5)	O2–Ni1–O3	176.35(9)
N2¹–Ni1–O2	93.26(5)	O2–Ni1–N1	97.50(10)
N2¹–Ni1–O3¹	80.37(5)	O2–Ni1–N2	80.50(10)
N1–Ni1–O2	80.54(5)	O3–Ni1–N1	80.89(9)
N1–Ni1–O3¹	94.09(6)	O3–Ni1–N2	96.63(10)
N1–Ni1–N2¹	102.46(7)	N2–Ni1–N1	102.93(10)
Ni1–O1–Ni1¹	97.20(5)	Ni1¹–O1–Ni1	96.56(9)

2			
Ga1–O1	1.995(2)	Ni1–O1	2.0287(19)
Ga1–O2	1.9998(19)	Ni1–O2	2.051(2)
Ga1–N8	1.974(2)	Ni1–O3	2.059(2)
Ga1–N5	1.959(2)	Ni1–O4	2.071(2)
Ga1–N4	2.142(2)	Ni1–N2	2.073(3)
Ga1–N3	2.149(2)	Ni1–N1	2.090(3)
O1–Ga1–O2	82.58(8)	O1–Ni1–O2	80.50(8)
O1–Ga1–N4	94.27(8)	O1–Ni1–O3	87.91(8)
O1–Ga1–N3	167.94(8)	O1–Ni1–O4	94.86(8)
O2–Ga1–N4	170.00(8)	O1–Ni1–N2	168.35(11)
O2–Ga1–N3	93.35(8)	O1–Ni1–N1	87.20(9)
N8–Ga1–O1	88.63(8)	O2–Ni1–O3	95.89(8)
N8–Ga1–O2	92.16(8)	O2–Ni1–O4	86.16(8)
N8–Ga1–N4	97.27(9)	O2–Ni1–N2	88.15(10)
N8–Ga1–N3	80.16(9)	O2–Ni1–N1	167.45(10)

N5–Ga1–O1	93.39(9)	O3–Ni1–O4	176.80(9)
N5–Ga1–O2	90.02(9)	O3–Ni1–N2	95.90(10)
N5–Ga1–N8	177.20(10)	O3–Ni1–N1	81.11(9)
N5–Ga1–N4	80.66(9)	O4–Ni1–N2	81.69(10)
N5–Ga1–N3	97.97(9)	O4–Ni1–N1	97.40(10)
N4–Ga1–N3	91.55(9)	N2–Ni1–N1	104.25(12)
Ga1–O1–Ni1	98.91(8)	Ga1–O2–Ni1	98.01(8)

Table S3. Distortion parameters for 1, 1' and 2.

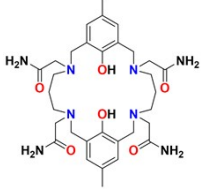
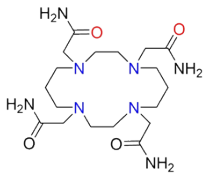
Complex	Temp	Ion	Σ/deg^a	Θ/deg^b
1	100.15 K	Ni1	64.6073	207.1362
	100.15 K	Ni2	64.6081	207.1367
1'	293(2) K	Ni1	62.5771	197.5625
2	100.0 K	Ni1	75.5658	205.1496
	100.0 K	Ga1	58.0180	195.4614

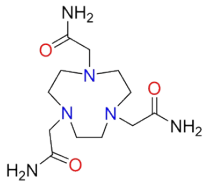
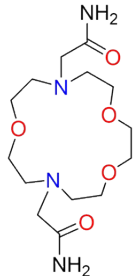
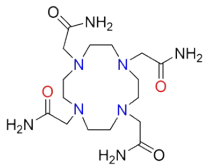
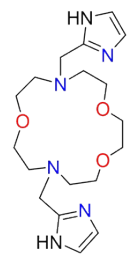
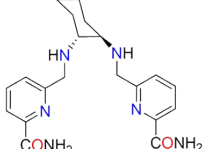
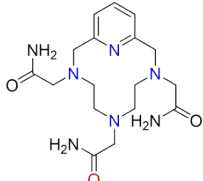
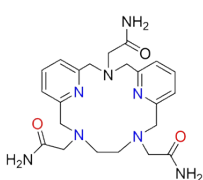
^a The sum of the deviation of 12 unique *cis* ligand-metal-ligand angles from 90°. ^b The sum of the deviation of 24 unique torsional angles between the ligand atoms on opposite triangular faces of the octahedron viewed along the *pseudo*-threefold axis from 60°.

Table S4. CShM analysis data for 1, 1' and 2.

Complex	Temp	Ion	Structure				
			HP-6	PPY-6	OC-6	TPR-6	JPPY-6
1	100.15 K	Ni	32.900	24.107	1.231	10.644	27.501
		Ni	32.900	24.107	1.231	10.644	27.500
1'	293(2) K	Ni	32.356	24.774	1.050	12.099	28.009
2	100.0 K	Ni	30.308	25.783	1.047	12.726	29.432
		Ga	29.812	26.329	0.979	14.019	29.980

Table S5. Comparison of % CEST of the Ni(II) analogues.

Complexes	Ligand	Chemical Shift (ppm)	CEST (%)	Conc. (mM)	N^a	m^b	Conditions
NiL		64	20%	10	8	4	9.4 T NMR, $B_1 = 24 \mu\text{T} \times 4 \text{ s}$, 37 °C, pH=7.4
Ni-CCRM ¹⁹		76	14	10	8	1	11.7 T NMR, $B_1 = 24 \mu\text{T} \times 2 \text{ s}$, 37 °C, pH=7.3

Ni-TCMT ¹⁹		76	13	10	6	3	11.7 T NMR, B ₁ = 24 μT×2 s, 37 °C, pH=7.4
Ni-NOPE ^{20,} 21		72	39 ± 0.2	10	4	2	11.7 T NMR, B ₁ = 24 μT×2 s, 37 °C, pH=7.4
Ni-TCMC ²²		76	6	10	8	4	11.7 T NMR, B ₁ = 24 μT×2 s, 37 °C, pH=7.5
Ni-HINO ²³		55	23 ± 1.3	8	2	1	11.7 T NMR, B ₁ = 24 μT×4 s, 37 °C, pH=7.2
Ni- chxdedpam ²⁴		83	~10%	15	4	2	7 T NMR, B ₁ = 25 μT×2 s, 37 °C, pH=7.2
Ni-TPTA ²⁵		70	5	10	2	2	9.4 T NMR, B ₁ = 25 μT×2 s, 37 °C, pH=7.4
Ni-DETA ²⁶		78	14	10	6	4	7 T NMR, B ₁ = 20 μT×3 s, 37 °C, pH=7.4

^a Total number of exchangeable protons in the paraCEST agent

^b Number of magnetically equivalent protons that give rise to a CEST peak

5. Additional Figures

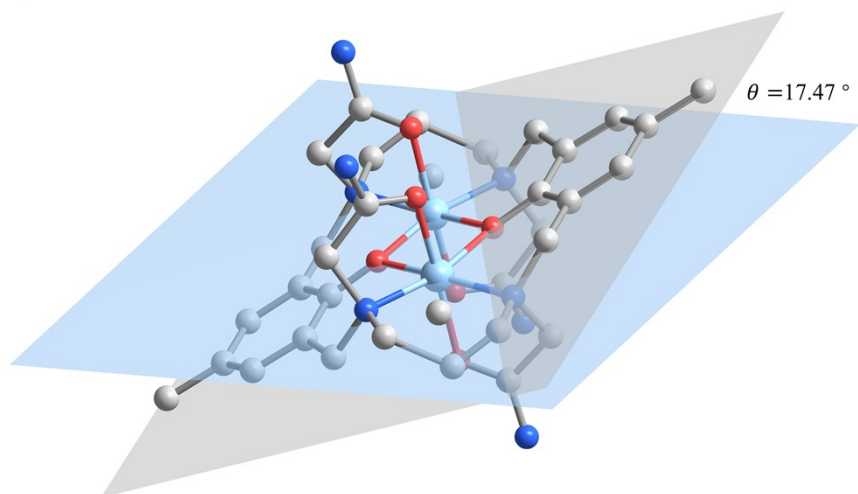


Fig. S1 The phenolato-ring and the Ni₂O₂ plane of **1** form a dihedral angle of 17.47°.

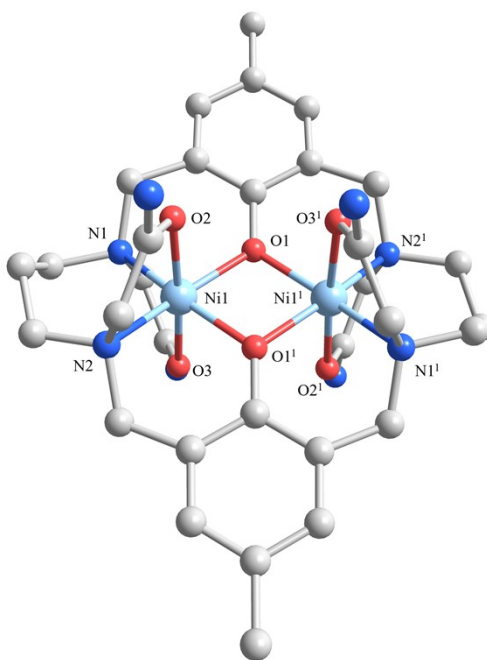


Fig. S2 Crystal structures of **1'**. Hydrogen atoms, solvent molecules, and counter anions are omitted for clarity. C, gray; N, blue; O, red; Ni, blue.

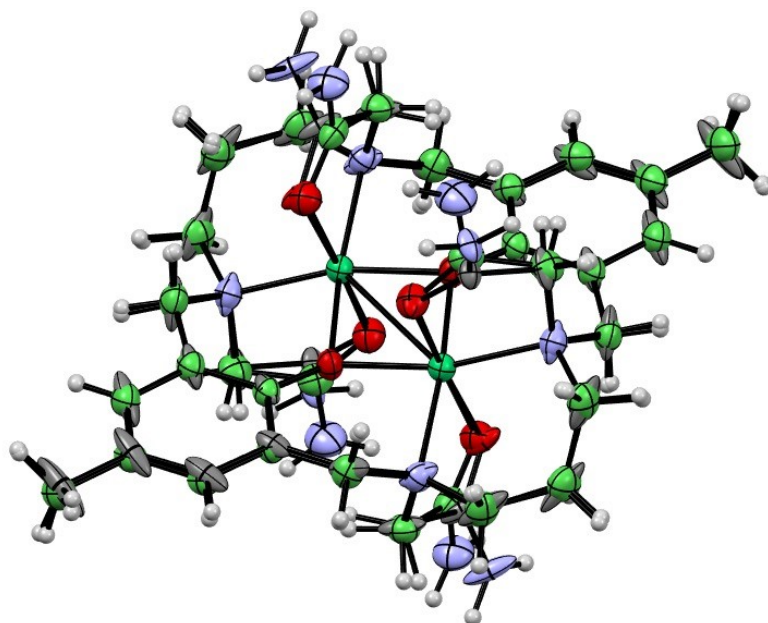


Fig. S3 Overlay of crystal structures for 1 and 1'. The main structural differences are located at the amide pendant arms. Notably, axial carboxamide arms display some structural differences, alluding to their propensity for deformative movements. The bond metrics for both structures are summarized in Table S2.

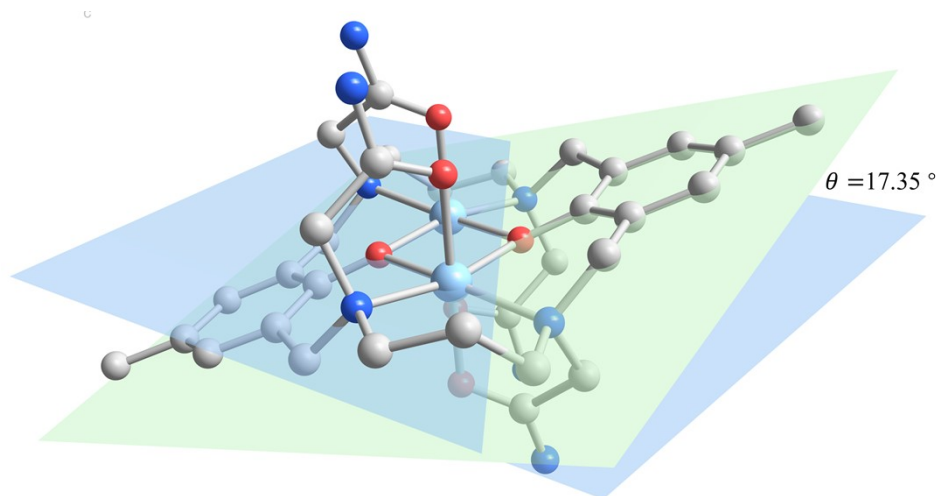


Fig. S4 The phenolato-ring and the Ni₂O₂ plane of 1' form a dihedral angle of 17.35°.

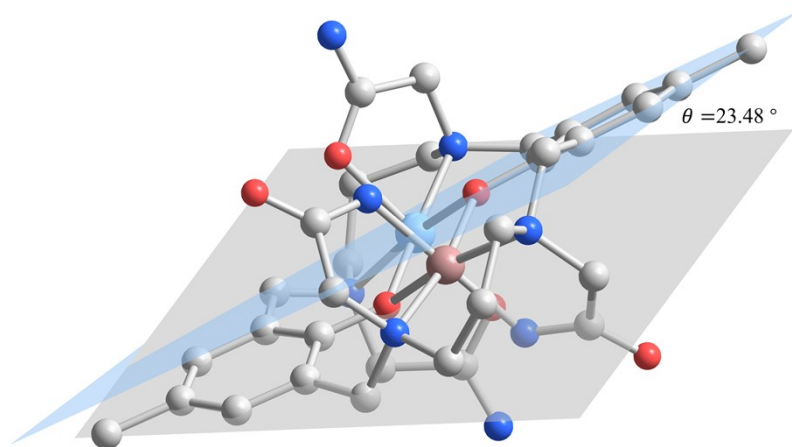


Fig. S5 The phenolato-rings of **2** form a dihedral angle of 23.48° .

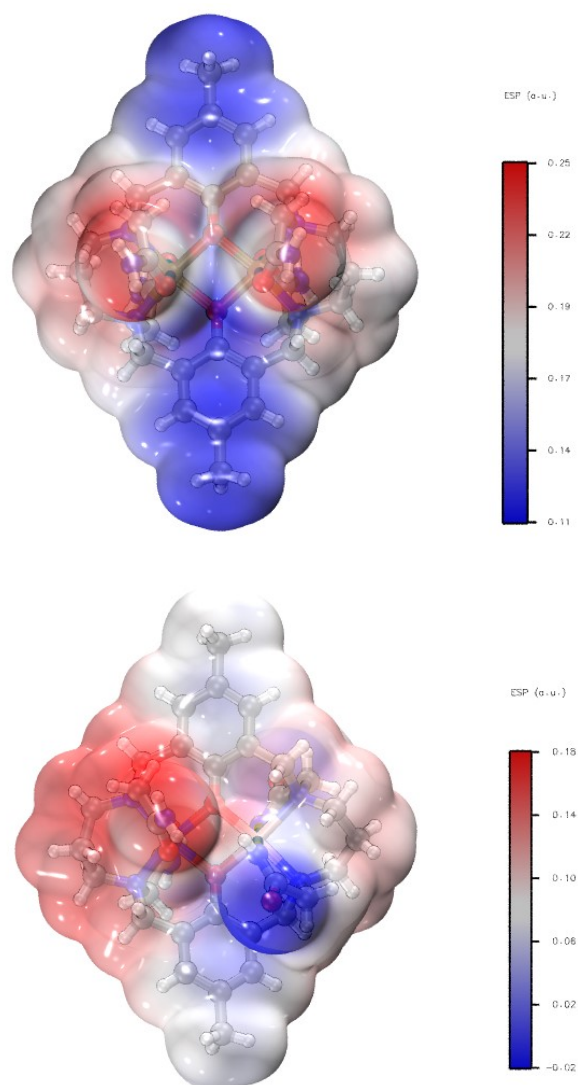


Fig. S6 Electrostatic potential (ESP) map of **1** (top) and **2** (bottom). (Isovalue: 0.001 a.u.)

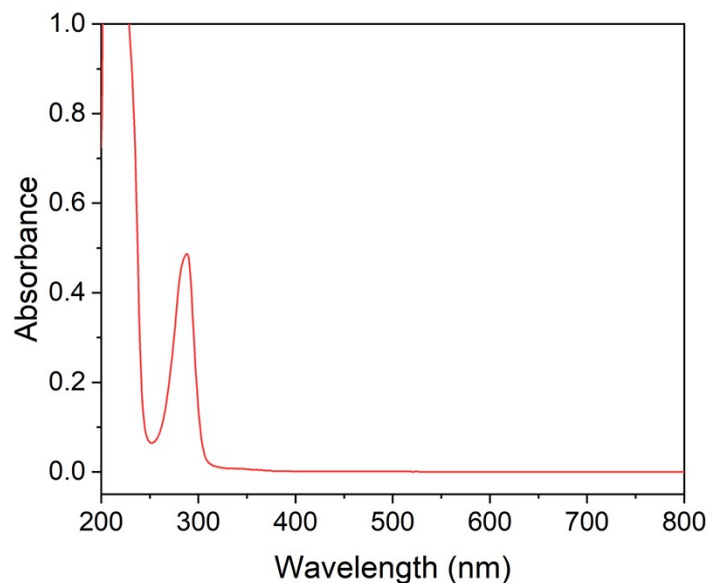


Fig. S7 UV-vis spectra of 0.10 mM of L in MeOH.

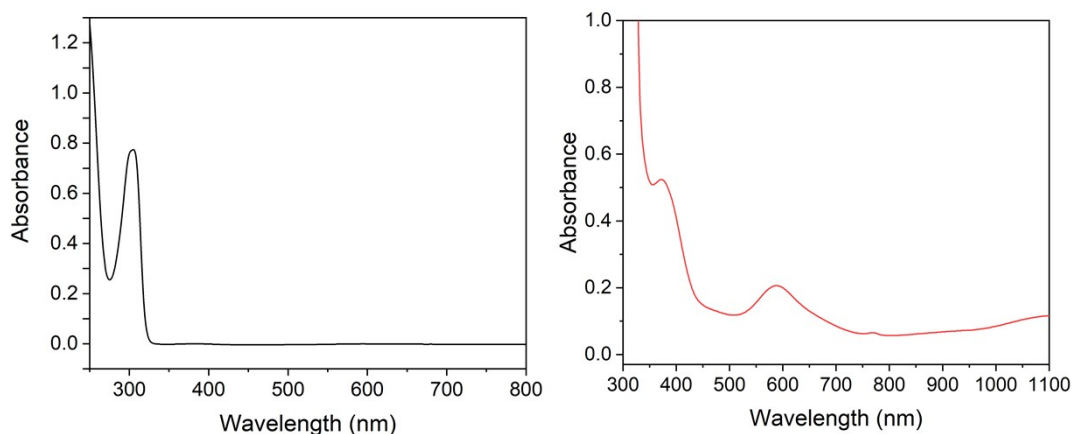


Fig. S8 UV-vis spectra of a solution containing 0.10 mM (left) and 5.0 mM (right) of 1 in 50 mM HEPES and 100 mM NaCl at pH 7.2. A strong absorption band at 305 nm ($\epsilon = 7197 M^{-1}cm^{-1}$) was observed, corresponding to the $n \rightarrow \pi^*$ transition of the phenolate groups, as confirmed by comparison with the UV-vis spectrum of the ligand itself, which showed a similar absorption peak at 288 nm ($\epsilon = 4728 M^{-1}cm^{-1}$) (Fig. S7). In addition, two other absorption features were detected at 380 nm ($\epsilon = 105 M^{-1}cm^{-1}$) and 570 nm ($\epsilon = 41.3 M^{-1}cm^{-1}$), ${}^3A_{2g} \rightarrow {}^3T_{1g}$ (P) and ${}^3A_{2g} \rightarrow {}^3T_{1g}$ (F) d-d transition bands, respectively (Fig. S8). A broad d-d transition band (${}^3A_{2g} \rightarrow {}^3T_{2g}$) was also present at approximately 1100 nm, which was beyond the measurable range of the spectrometer (Fig. S8).

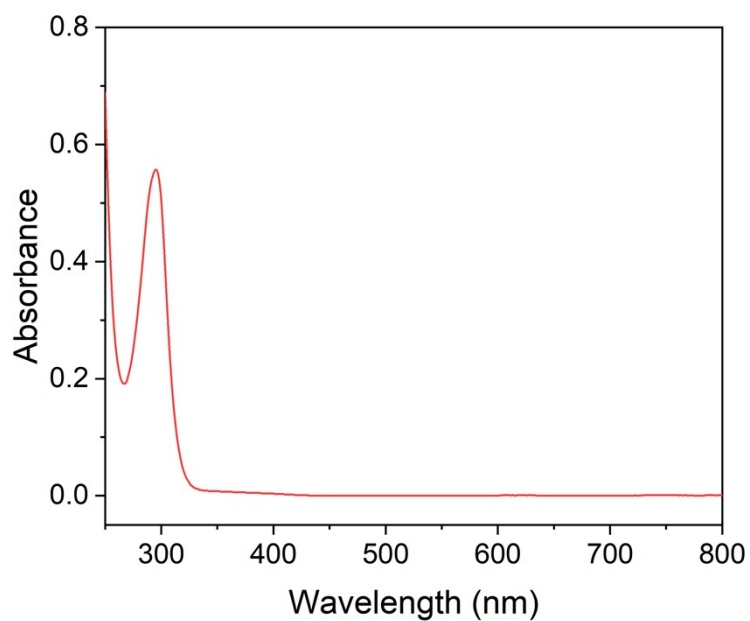


Fig. S9 UV-vis spectrum of a solution containing 0.10 mM of **2** in 50 mM HEPES and 100 mM NaCl at pH 7.2.

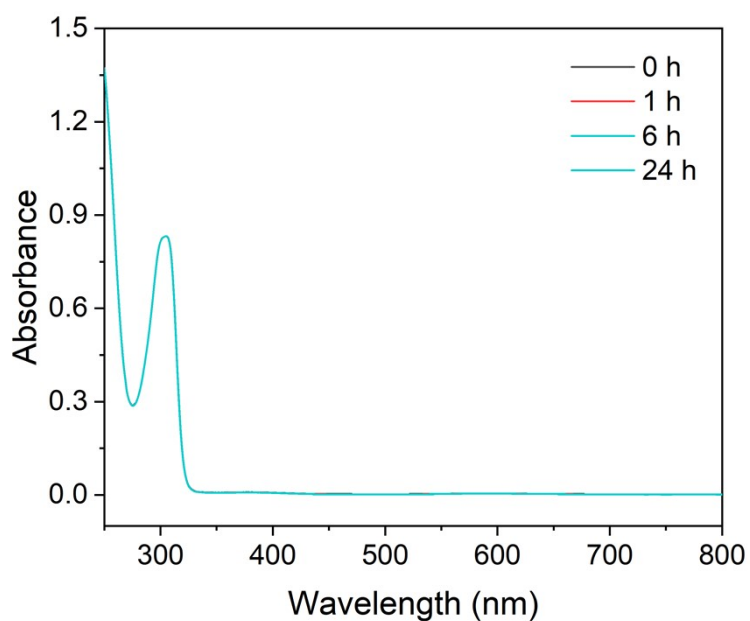


Fig. S10 UV-vis spectra of a solution containing 0.10 mM of **1** in 50 mM HEPES and 100 mM NaCl at pH 7.2, the solution was scanned immediately after the addition of 5 mM CaCl₂.

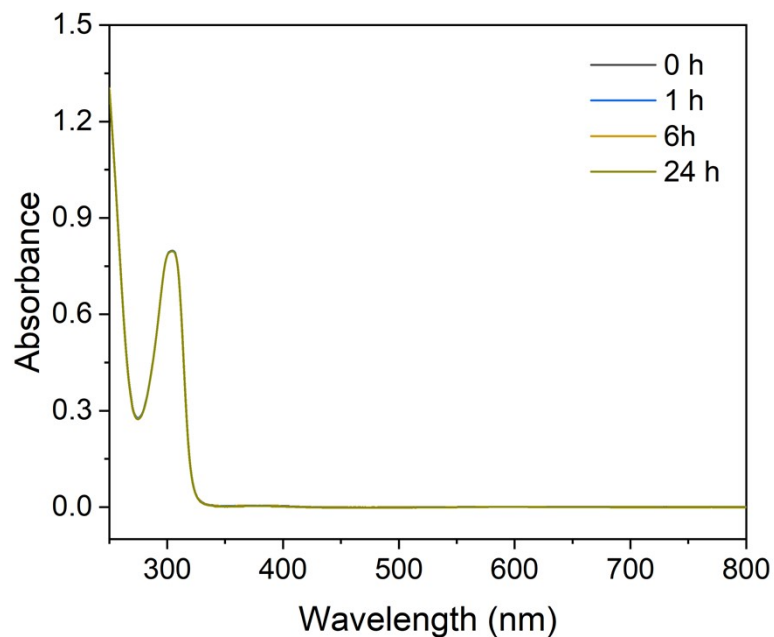


Fig. S11 UV-vis spectra of a solution containing 0.10 mM of **1** in 50 mM HEPES and 100 mM NaCl at pH 7.2, the solution was scanned immediately after the addition of 4 mM ZnCl₂.

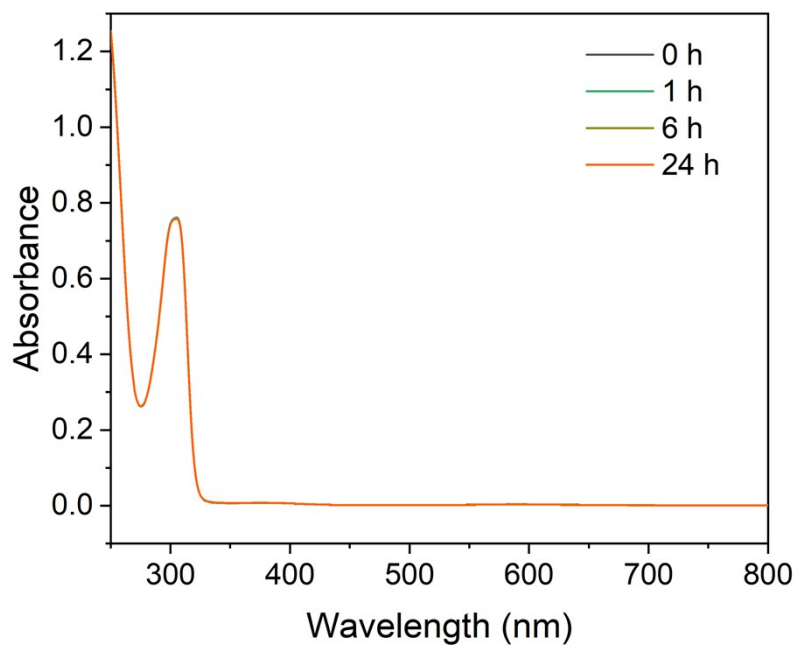


Fig S12 UV-vis spectra of a solution containing 0.10 mM of **1** in 50 mM HEPES and 100 mM NaCl at pH 7.2, the solution was scanned immediately after the addition of 4 mM Na₂CO₃ and NaH₂PO₄.

Table S6. Protonation and stability constants of ligand and Ni(II) complex (I = 0.15 M NaCl and T = 25 °C)

<i>h</i>	$\log\beta_h$	$pK_a(H_hL)$	<i>h</i>	<i>l</i>	<i>m</i>	$\log\beta_{hlm}$	$pK_a(H_hLNi_m)$	$\log K(H_hLNi_m)$
1	13.40(6)	13.40(6)	-1	1	1	2.53(2)	–	–
2	25.79(8)	12.39(8)	0	1	1	13.82(4)	11.3(4)	13.82(4)
3	32.53(7)	6.74(8)	1	1	1	24.29(4)	10.46(4)	10.89(6)
4	38.66(4)	6.13(7)	2	1	1	31.86(2)	7.57(4)	6.07(8)
5	42.18(7)	3.52(7)	3	1	1	36.65(3)	4.79(3)	4.12(7)
6	45.51(3)	3.33(7)	-2	1	2	1.54(5)	–	–
			-1	1	2	12.57(3)	11.03(5)	–
			0	1	2	21.97(2)	9.40(3)	8.15(4)
			1	1	2	29.01(2)	7.04(2)	4.72(6)
			2	1	2	34.89(2)	5.88(2)	3.03(8)

$$\beta_h = [H_hL] / \{[H]^h \cdot [L]\} \quad K_a(H_hL) = [H_hL] / \{[H] \cdot [H_{h-1}L]\}$$

$$\beta_{hlm} = [H_hL_lNi_m] / \{[H]^h \cdot [L]^l \cdot [Ni]^m\} \quad K_a(H_hLNi_m) = [H_hLNi_m] / \{[H] \cdot [H_{h-1}LNi_m]\}$$

$$K(H_hLNi_m) = [H_hLNi_m] / \{[Ni] \cdot [H_hLNi_{m-1}]\}$$

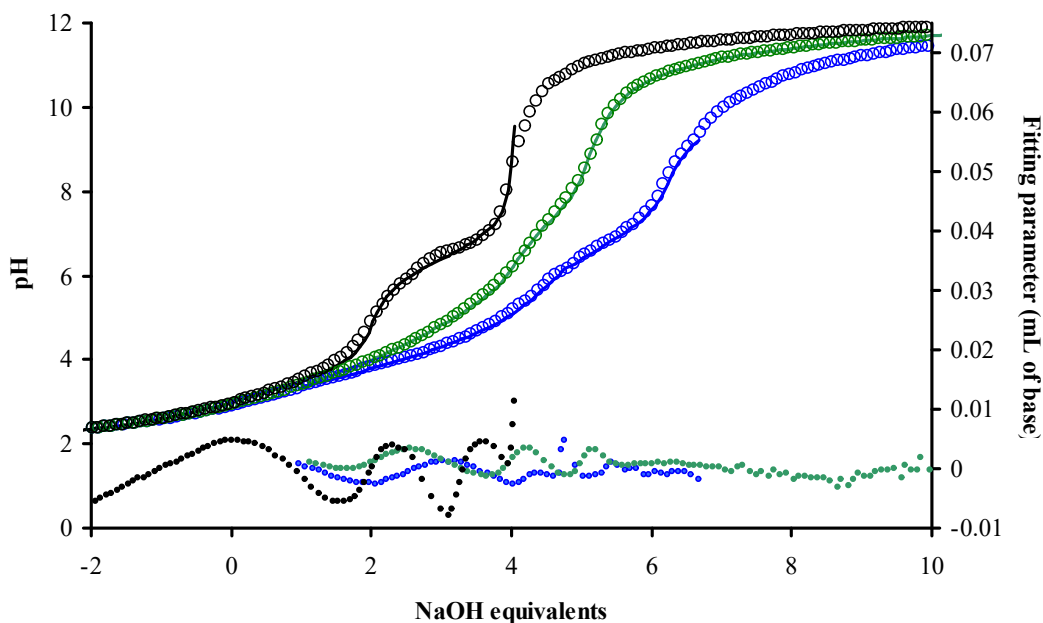


Fig. S13 pH-potentiometric titration curve of 1.96 mM ligand in the absence (black dots) and in the presence of one (green) and two equivalents (blue) of NiCl_2 ($I=0.15$ M NaCl, $T=25$ °C). Lines represent the fitted curves by the PSEQUAD program. Their average difference values are: 5.28×10^{-3} , 3.37×10^{-3} and 3.28×10^{-3} for the ligand (black), 1:1 Ni:L (green) and 2:1 Ni:L (blue) titration samples, respectively.

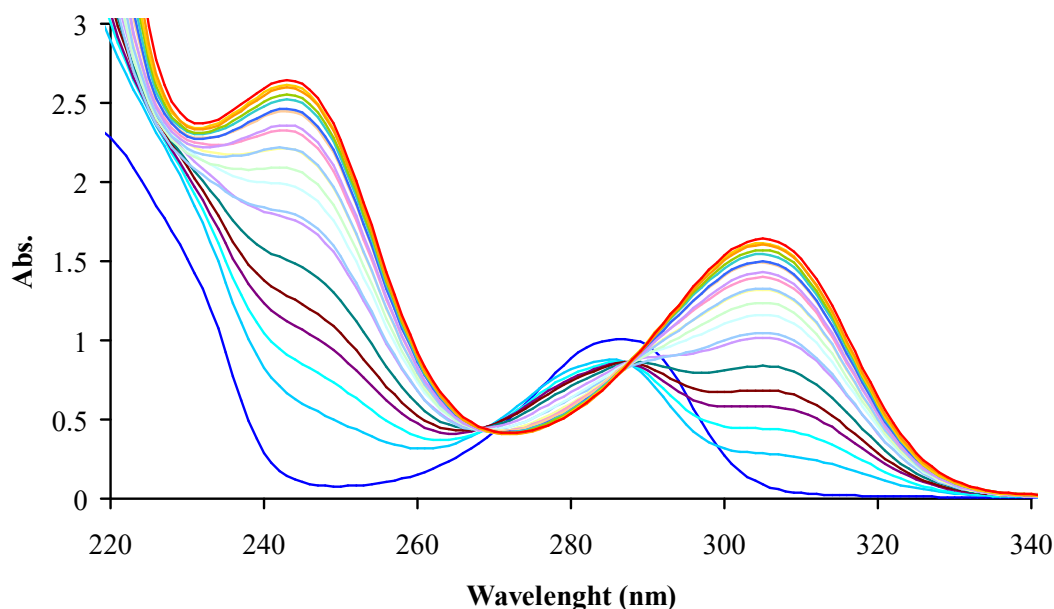


Fig. S14 Spectral changes observed upon titrating of 0.164 mM ligand with NaOH ($I=0.15$ M NaCl, $T=25$ °C). The concentration of NaOH in the sample are as follows: -0.0005049, 0.006841, 0.01419, 0.02153, 0.02888, 0.04357, 0.07296, 0.08765, 0.10969, 0.15376, 0.18315, 0.21253, 0.25661, 0.33007, 0.40353, 0.47699, 0.57983, 0.72675, 0.88836, 1.0353, 1.3291 M. The average difference between the measured and fitted absorbance is 3.28×10^{-2} .

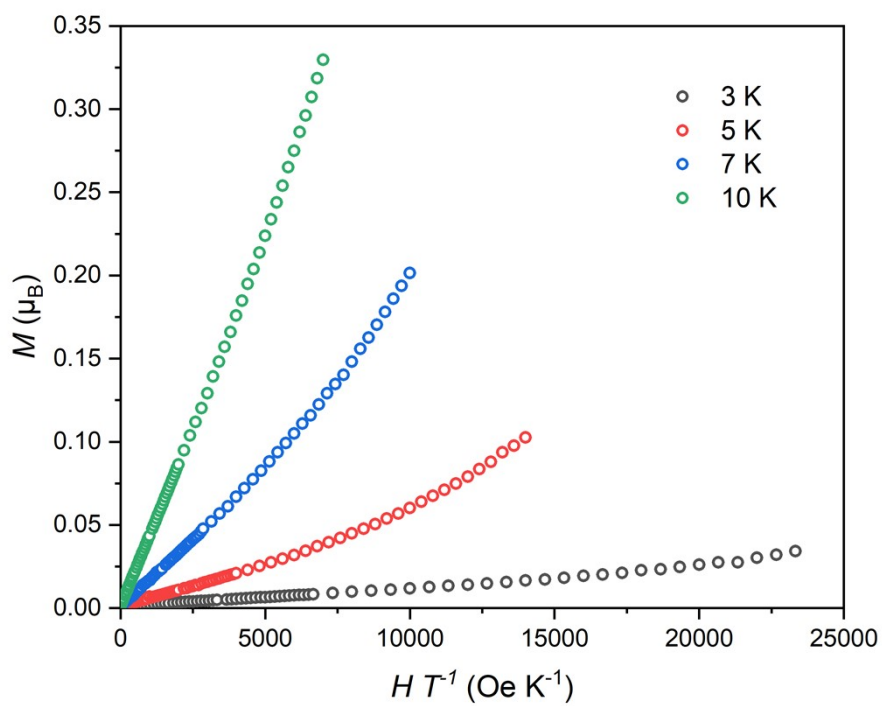
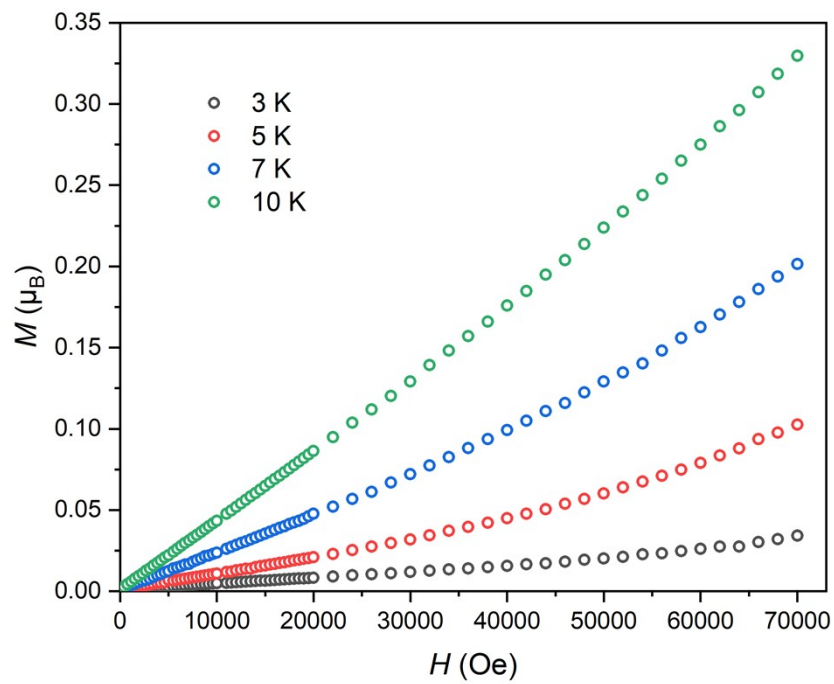


Fig. S15 Magnetization and reduced magnetization curves of **1** at the respective temperatures.

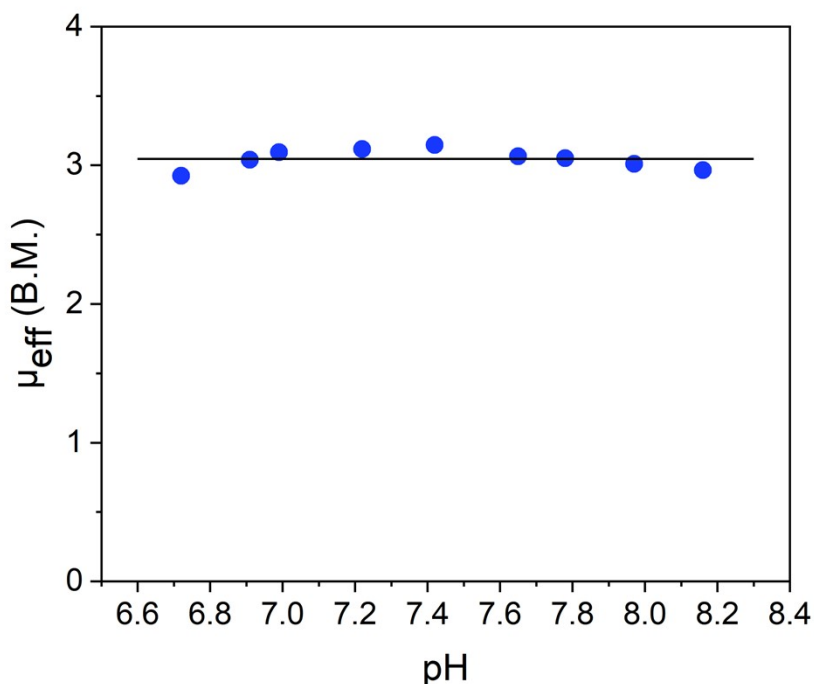


Fig. S16 Variable-pH magnetic susceptibility data for 1 in aqueous solutions containing 50 mM HEPES and 100 mM NaCl at 25 °C, obtained using the Evans method (see Equation S2 in the Experimental Section of the manuscript). The solid black line denotes the average value of $\chi_M T = 3.06 \text{ cm}^3 \text{ K mol}^{-1}$.

Table S7. Peak positions, T_1 Values, distances of hydrogens to Ni, and tentative assignments for **1** recorded under 500 MHz at 37 °C.

Chemical Shift (ppm)	T_1 (ms)	Linewidth ^a (Hz)	$r_{\text{Ni-H}}$ ^b (Å)	Proton assignment
186.2	0.81±0.01	1274	4.44	3
114.7	0.78±0.01	1181	3.61	5
63.8	0.22±0.01	1509	4.34	4
20.7	3.48±0.02	104	5.77	2
9.4	0.26±0.01	1168	4.34	4
1.5	16.16±0.02	24	7.52	1
-9.5	0.52±0.01	654	5.06	6

^a The linewidths are full width at half-maximum. ^b The metal-proton distances are average distances measured from X-ray crystal structure.

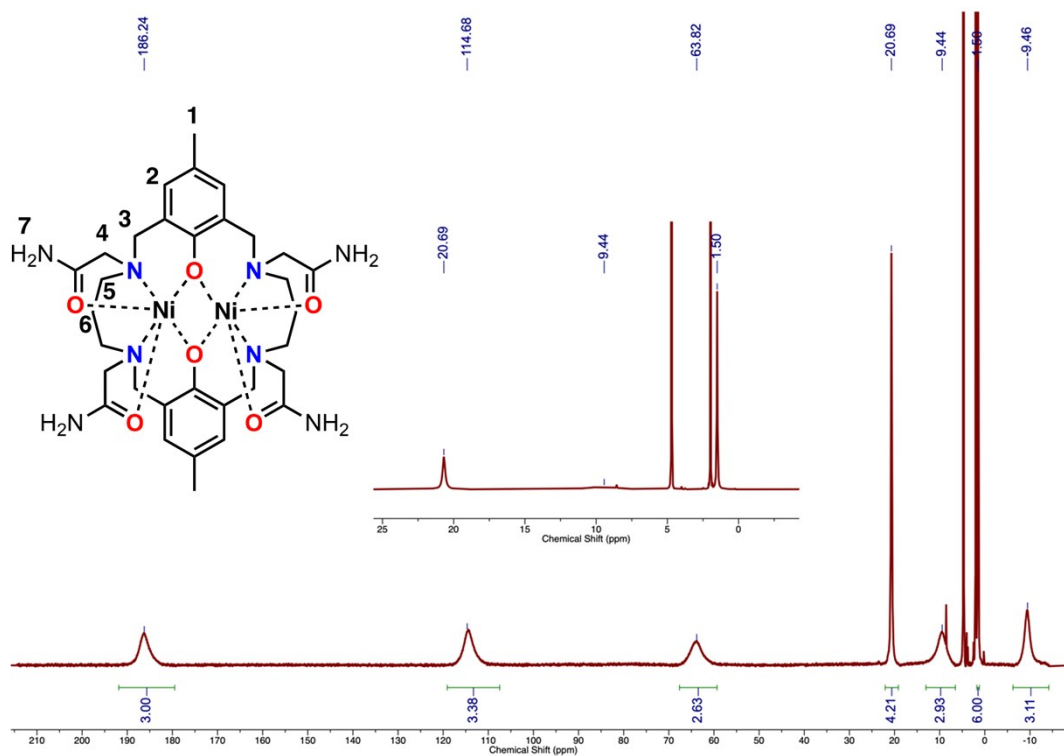


Fig. S17 500 MHz ^1H NMR spectrum of **1** in D_2O at 310 K.

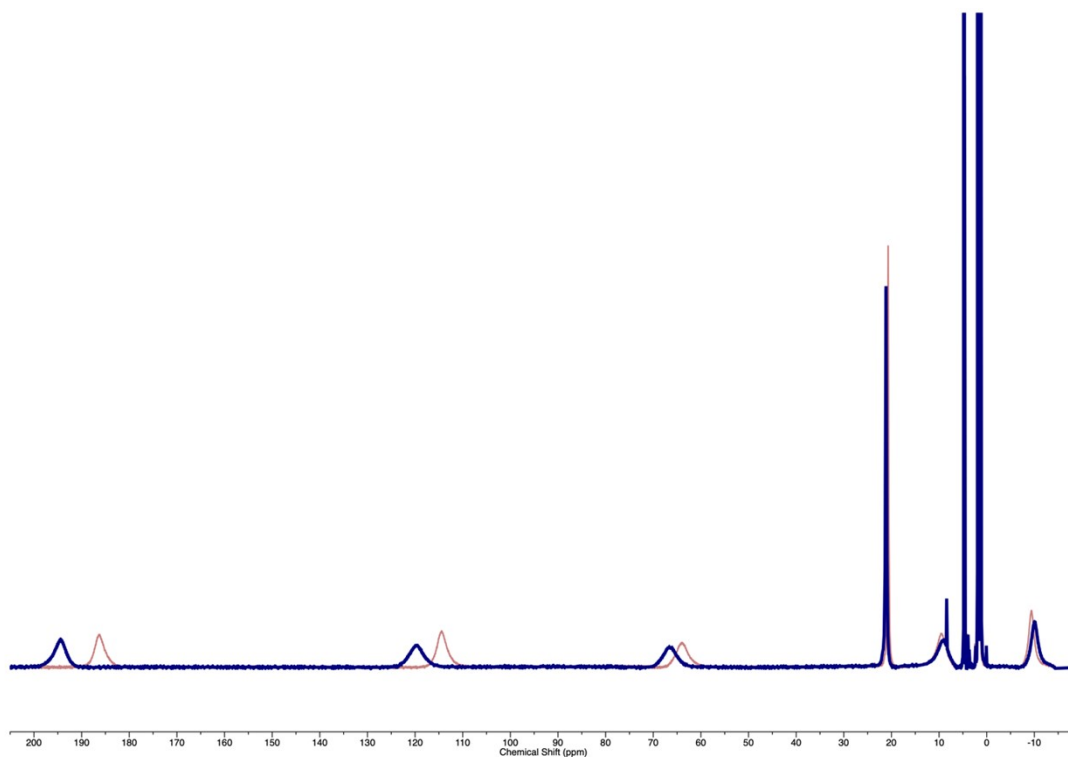


Fig. S18 500 MHz ^1H NMR spectra of **1** in D_2O at 298 K (navy) and 310 K (maroon).

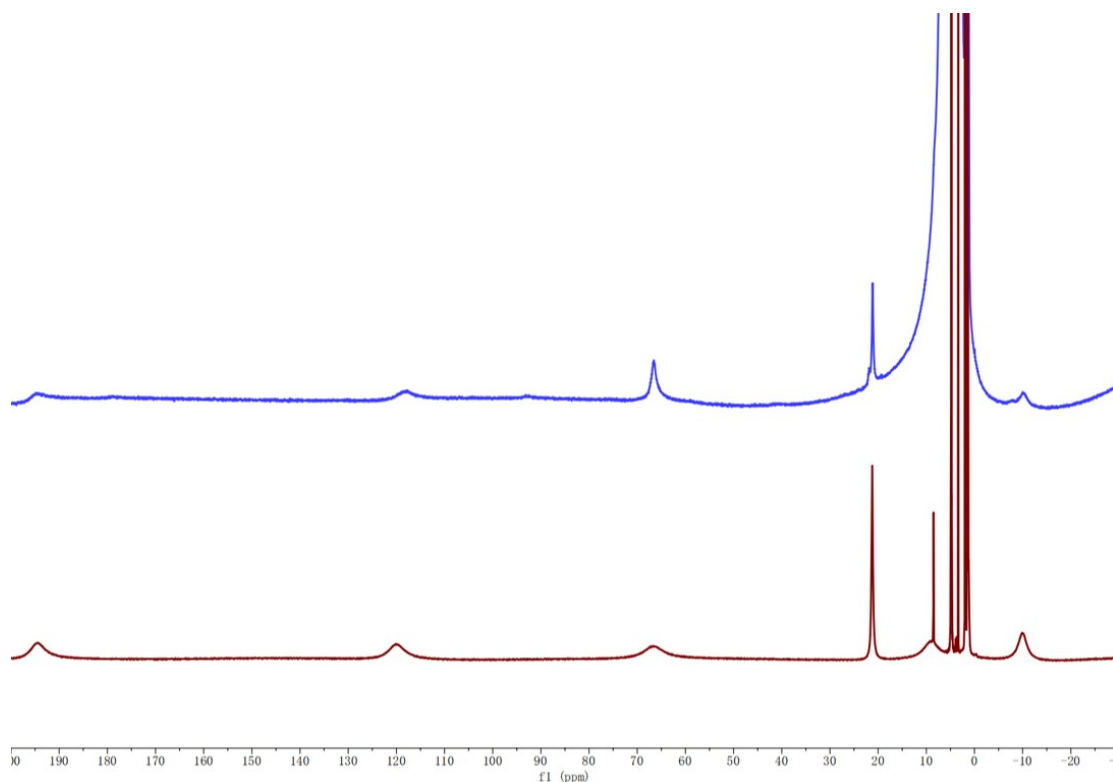


Fig. S19 400 MHz ^1H NMR spectrum of **1** in D_2O (red) and 50 mM HEPES and 100 mM NaCl at pH 7.2 (blue).

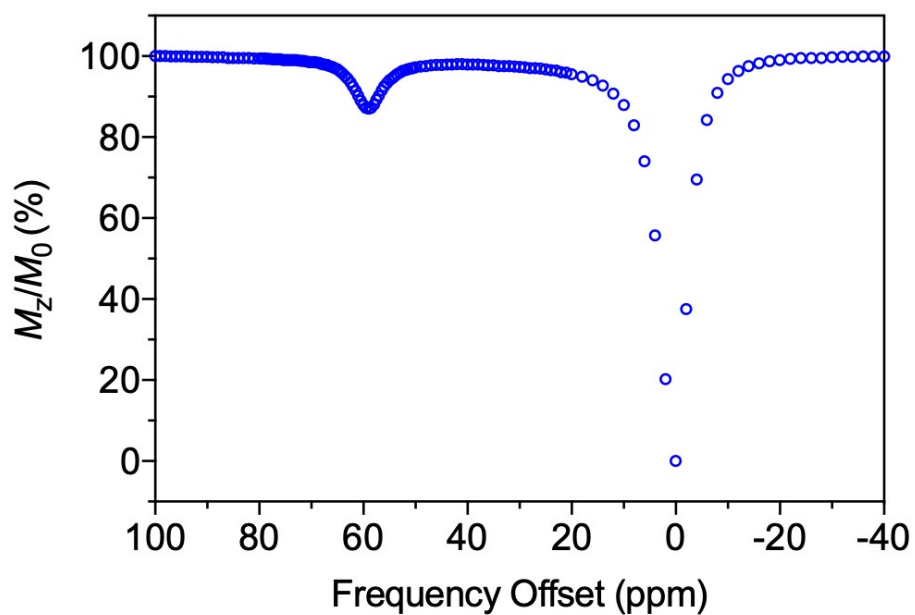


Fig. S20 CEST spectrum recorded at 9.4 T of 10 mM **1** in 50 mM HEPES buffer solution at pH 7.15 and 37 $^\circ\text{C}$, with a 4 s presaturation pulse of 24 μT .

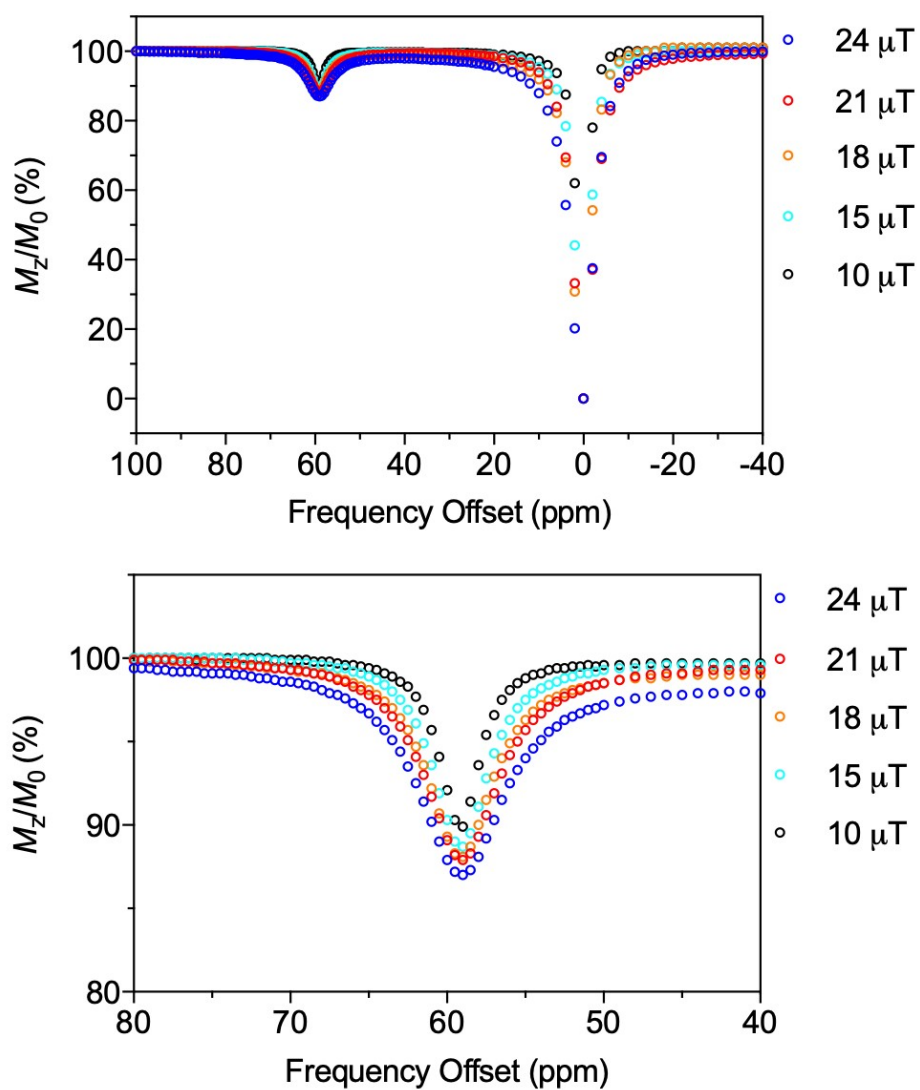


Fig. S21 CEST spectra recorded at 9.4 T of 10 mM **1** in 50 mM HEPES buffer solution at pH 7.15 and 37 °C, with a 4 s presaturation pulse from 10 to 24 μT .

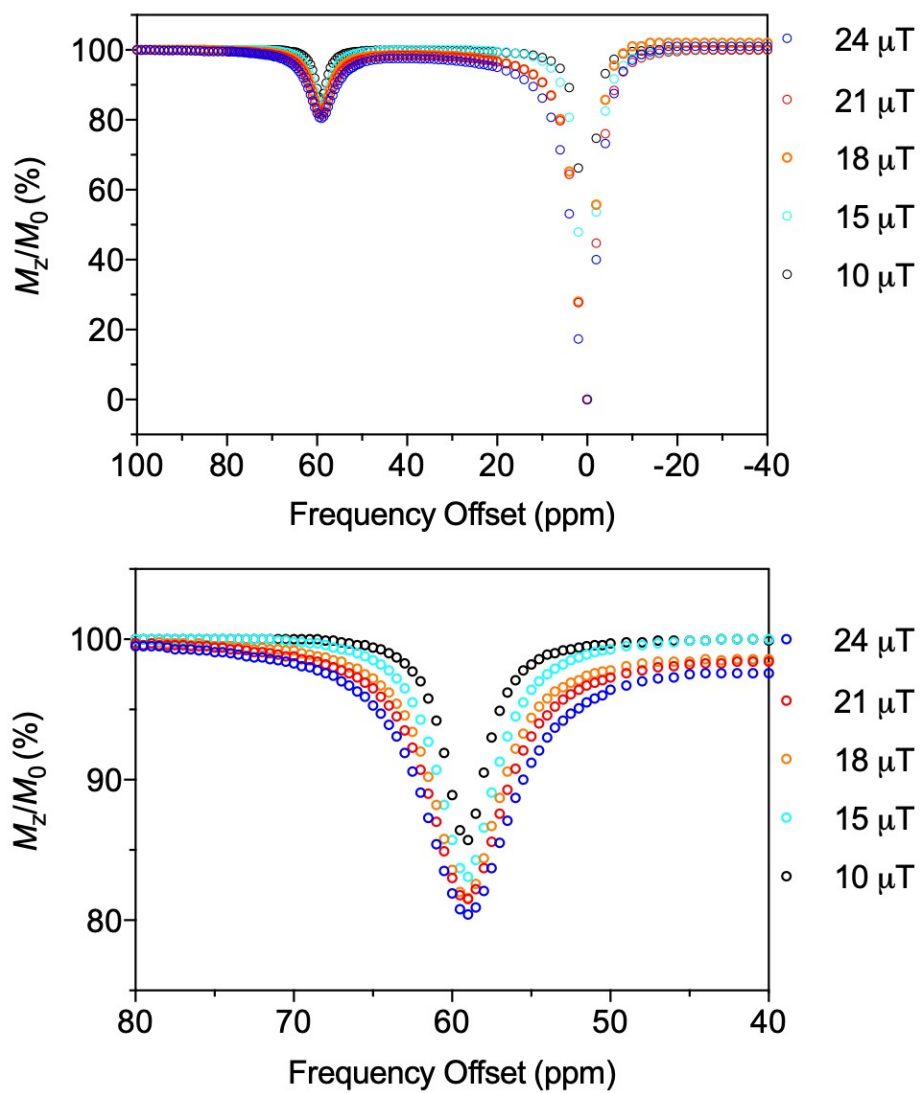


Fig. S22 CEST spectra recorded at 9.4 T of 10 mM **1** in 50 mM HEPES buffer solution at pH 7.40 and 37 °C, with a 4 s presaturation pulse from 10 to 24 μT .

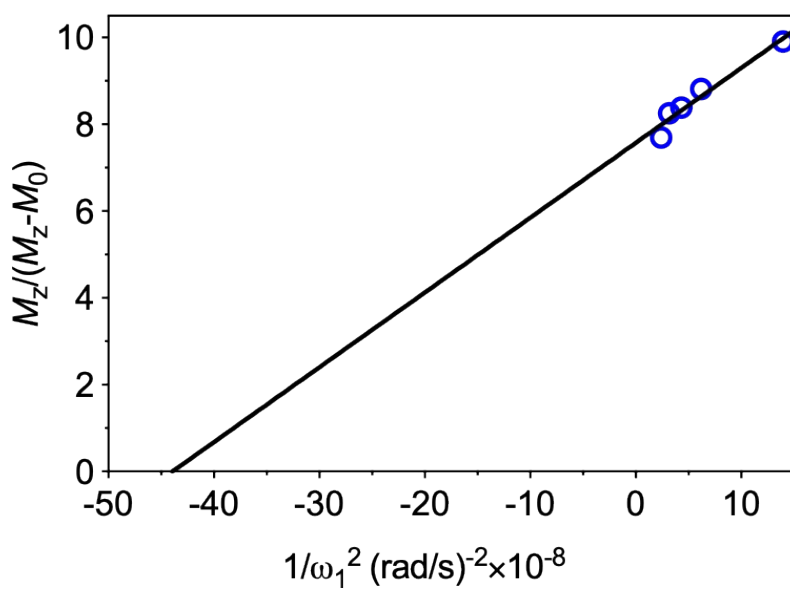


Fig. S23 Omega plot of 10 mM **1** in 50 mM HEPES buffer solution at pH 7.15 and 37 °C.

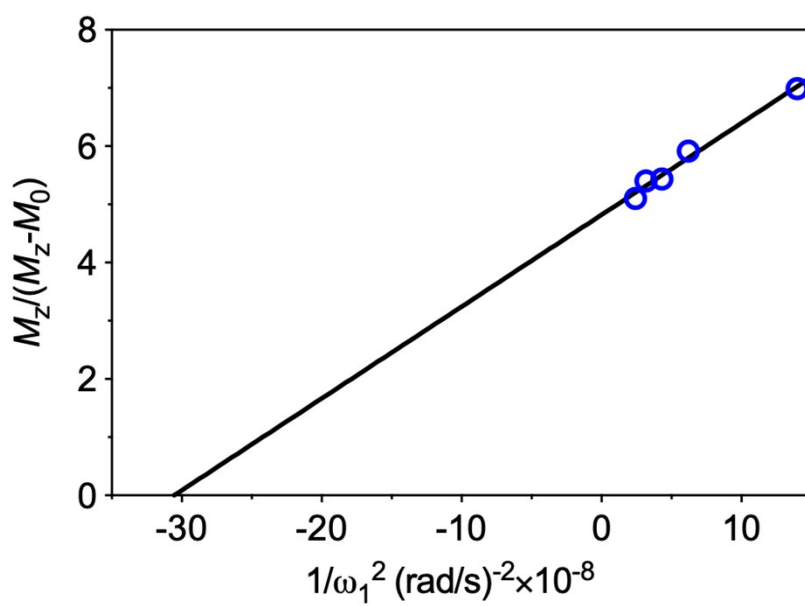


Fig. S24 Omega plot of 10 mM **1** in 50 mM HEPES buffer solution at pH 7.40 and 37 °C.

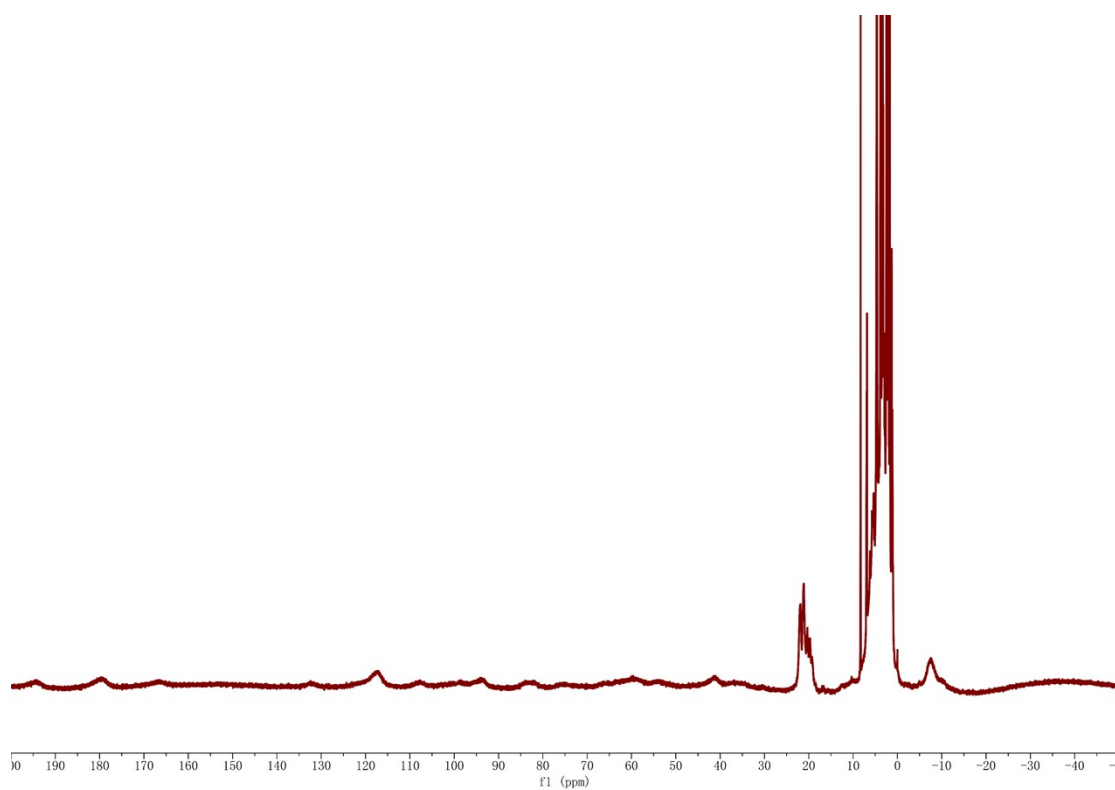


Fig. S25 400 MHz ^1H NMR spectrum of **2** in D_2O .

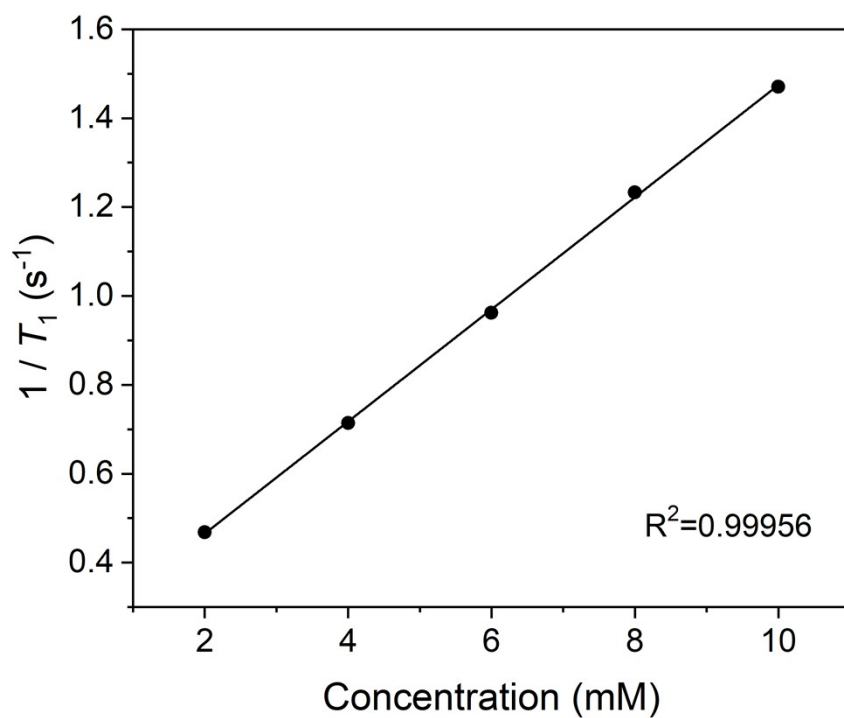


Fig. S26 Plots of $(1/T_1)$ versus concentration of **1**. R_1 value of $0.126 \pm 0.001 \text{ mM}^{-1}\text{s}^{-1}$ for **1** was determined.

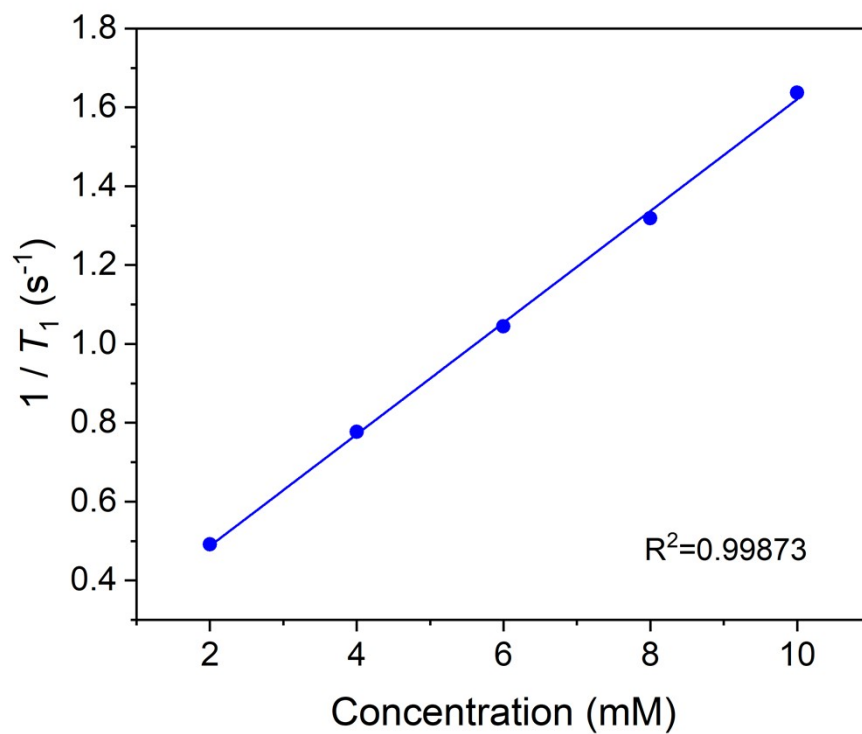


Fig. S27 Plots of $(1/T_1)$ versus concentration of **2**. R_1 value of $0.142 \pm 0.003 \text{ mM}^{-1}\text{s}^{-1}$ for **2** was determined.

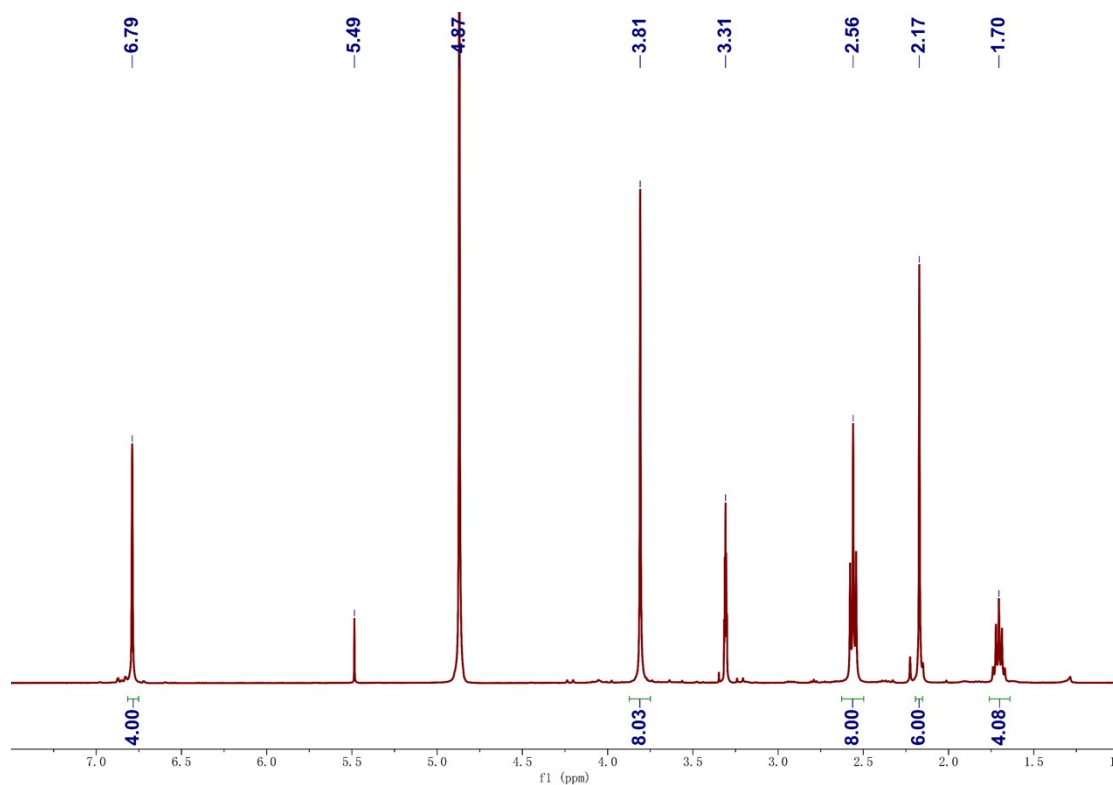


Fig. S28 400 MHz ^1H NMR spectrum of **C3-N** in CD_3OD .

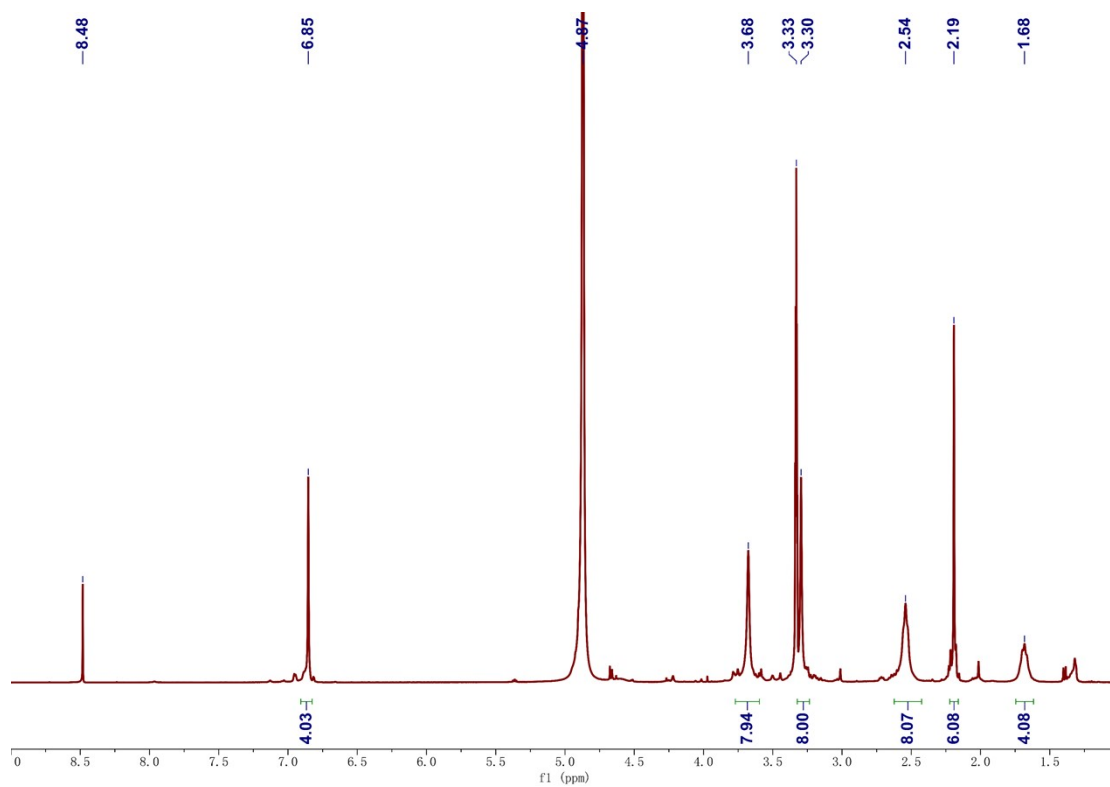


Fig. S29 400 MHz ^1H NMR spectrum of **L** in CD_3OD .

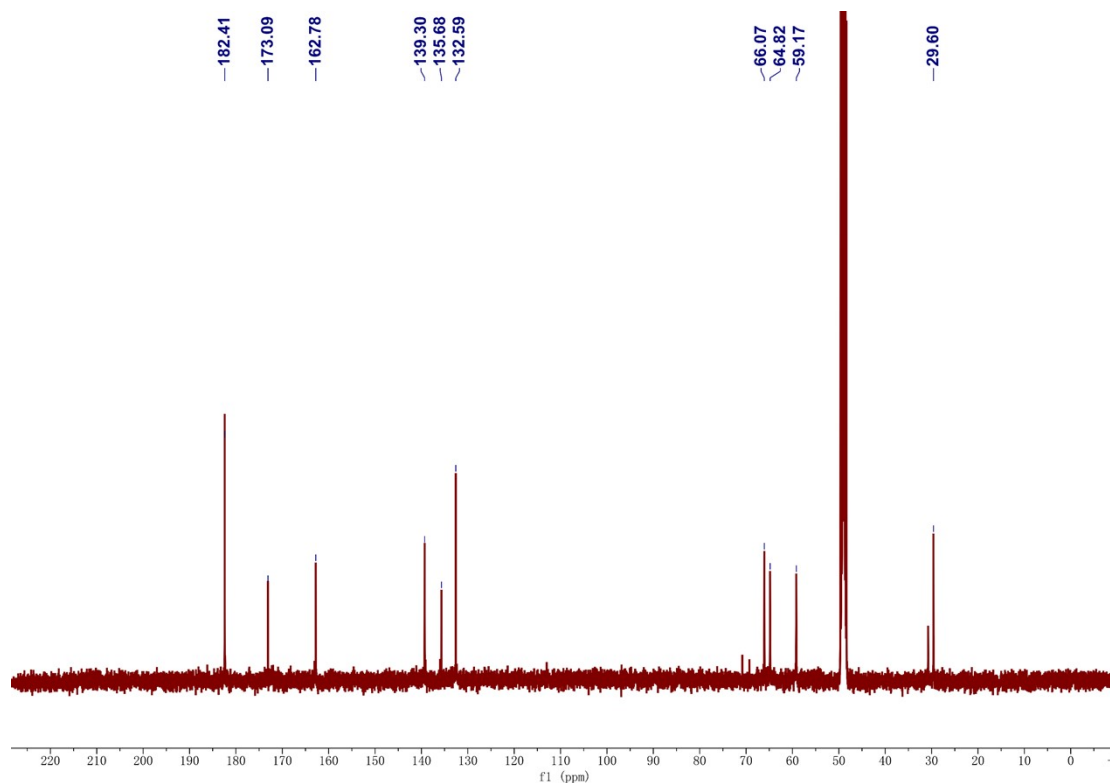


Fig. S30 100 MHz ^{13}C NMR spectrum of **L** in DMSO-d_6 .

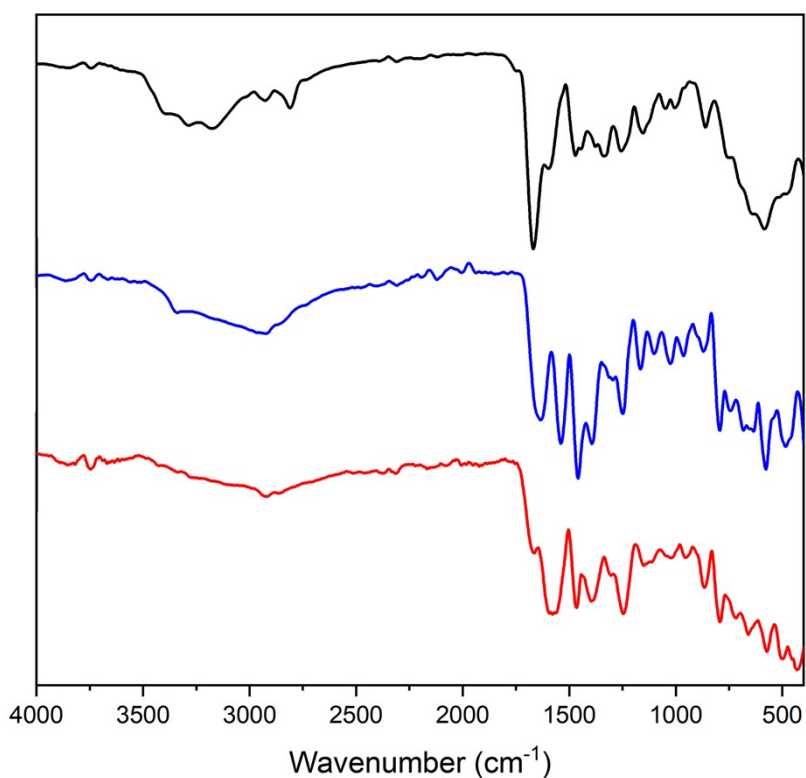


Fig. S31 IR spectra of solid state samples of **L** (top), **1** (middle), and **2** (bottom).

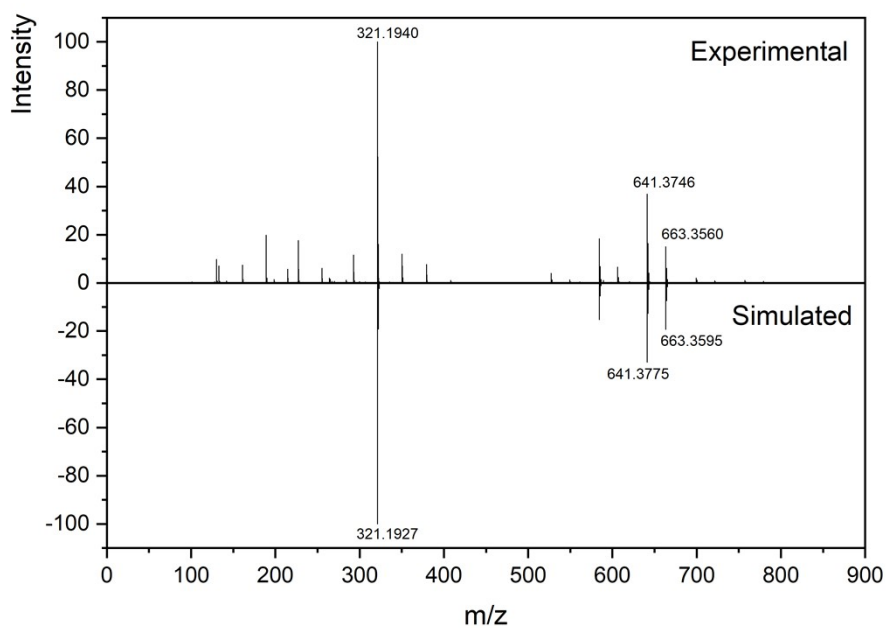


Fig. S32 Mass spectrum (ESI) for **L** in MeCN. The 321.1294 m/z feature is assigned to $[(L+2H)]^{2+}$ (calculated m/z = 321.1927). The 641.3746 m/z feature is assigned to $[L+H]^+$ (calculated m/z = 641.3775). The 663.3560 m/z feature is assigned to $[L+Na]^+$ (calculated m/z = 663.3595).

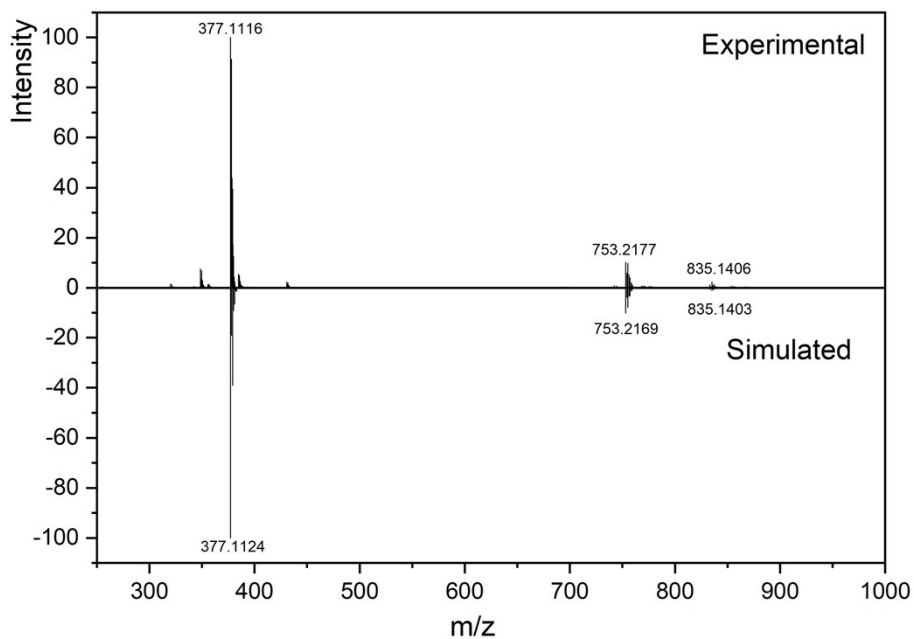


Fig. S33 Mass spectrum (ESI) for **1** in MeOH. The 377.1116 m/z feature is assigned to $[L+2M+H]^{2+}$ (calculated m/z = 377.1124). The 753.2177 m/z feature is assigned to $[L+2M]^+$ (calculated m/z = 753.2169). The 835.1406 m/z feature is assigned to $[L+2M+Br]^+$ (calculated m/z = 835.1403).

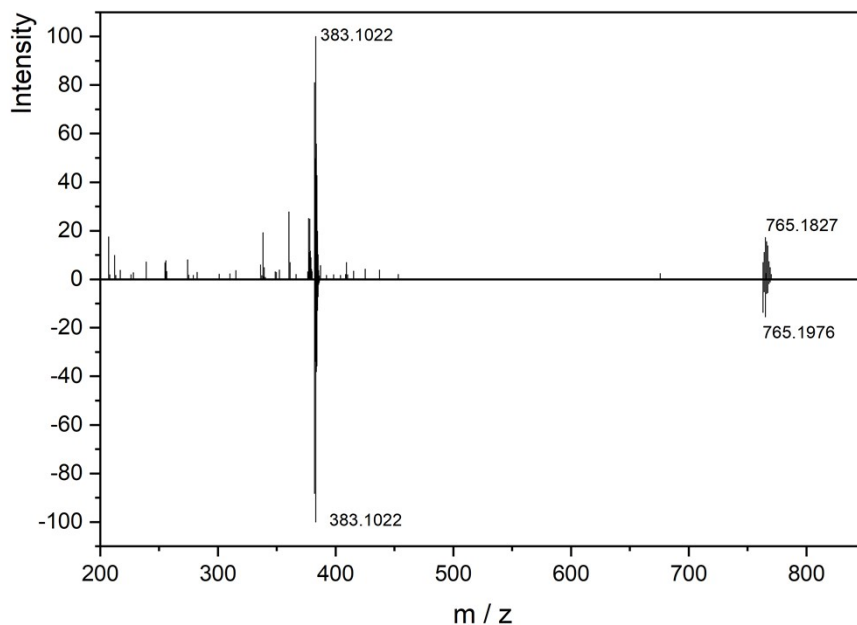


Fig. S34 Mass spectrum (ESI) for **2** in MeOH. The 383.1022 m/z feature is assigned to $[L+2M+H]^{2+}$ (calculated m/z = 383.1022). The 765.1827 m/z feature is assigned to $[L+2M+2H]^+$ (calculated m/z = 765.1976).

6. References

- 1 D. F. Evans, *J. Chem. Soc.*, 1959, **81**, 2003–2005.
- 2 D. Montagner, V. Gandin, C. Marzano and A. Erxleben, *Eur. J. Inorg. Chem.*, 2014, **2014**, 4043–4049.
- 3 W. T. Dixon, J. Ren, A. J. Lubag, J. Ratnakar, E. Vinogradov, I. Hancu, R. E. Lenkinski and A. D. Sherry, *Magn Reson Med.*, 2010, **63**, 625–632.
- 4 G. M. Sheldrick, *Acta Cryst.*, 2015, **C71**, 3–8.
- 5 O. V. Dolomanov, L. J. Bourhis, R. J. Gildea, J. A. K. Howard and H. Puschmann, *J. Appl. Cryst.*, 2009, **42**, 339–341.
- 6 H. M. Irving, M. G. Miles and L. D. Pettit, *Anal. Chim. Acta*, 1967, **38**, 475–488.
- 7 L. Zekany and I. Nagypal, in *Computational Methods for the Determination of Formation Constants*, ed. D. J. Leggett, Springer US, Boston, MA, 1985, pp. 291–353.
- 8 P. D. Knight, A. J. White and C. K. Williams, *Inorg. Chem.*, 2008, **47**, 11711–11719.
- 9 A. E. Thorarinsdottir, S. M. Tatro and T. D. Harris, *Inorg. Chem.*, 2018, **57**, 11252–11263.
- 10 F. Neese, *Wiley Interdiscip. Rev.: Comput. Mol. Sci.*, 2022, **12**, e1606.
- 11 A. Bencini and D. Gatteschi, *J. Am. Chem. Soc.*, 1986, **108**, 5763–5771.
- 12 C. Lee, W. Yang and R. G. Parr, *Phys. Rev. B.*, 1988, **37**, 785–789.
- 13 F. Neese, F. Wennmohs, A. Hansen and U. Becker, *Chem. Phys.*, 2009, **356**, 98–109.
- 14 K. Eichkorn, O. Treutler, H. Öhm, M. Häser and R. Ahlrichs, *Chem. Phys. Lett.*, 1995, **240**, 283–290.
- 15 K. Eichkorn, F. Weigend, O. Treutler and R. Ahlrichs, *Theor Chem Acc.*, 1997, **97**, 119–124.
- 16 A. P. Ginsberg, *J. Am. Chem. Soc.*, 1980, **102**, 111–117.
- 17 J. K. S. Wan, J. Dobkowski and N. J. Turro, *Chem. Phys. Lett.*, 1986, **131**, 129–133.
- 18 T. Soda, Y. Kitagawa, T. Onishi, Y. Takano, Y. Shigeta, H. Nagao, Y. Yoshioka and K. Yamaguchi, *Chem. Phys. Lett.*, 2000, **319**, 223–230.
- 19 S. J. Dorazio, A. O. Olatunde, P. B. Tsitovich and J. R. Morrow, *J Biol Inorg Chem*, 2014, **19**, 191–205.
- 20 A. O. Olatunde, J. M. Cox, M. D. Daddario, J. A. Sperryak, J. B. Benedict and J. R. Morrow, *Inorg. Chem.*, 2014, **53**, 8311–8321.
- 21 A. O. Olatunde, S. J. Dorazio, J. A. Sperryak and J. R. Morrow, *J. Am. Chem. Soc.*, 2012, **134**, 18503–18505.
- 22 A. O. Olatunde, C. J. Bond, S. J. Dorazio, J. M. Cox, J. B. Benedict, M. D. Daddario, J. A. Sperryak and J. R. Morrow, *Chem. Eur. J.*, 2015, **21**, 18290–18300.
- 23 P. J. Burns, J. M. Cox and J. R. Morrow, *Inorg Chem.*, 2017, **56**, 4545–4554.
- 24 L. Caneda-Martinez, L. Valencia, I. Fernandez-Perez, M. Regueiro-Figueroa, G. Angelovski, I. Brandariz, D. Esteban-Gomez and C. Platas-Iglesias, *Dalton Trans.*, 2017, **46**, 15095–15106.
- 25 R. N. Pradhan, S. Chakraborty, P. Bharti, J. Kumar, A. Ghosh and A. K. Singh, *Dalton Trans.*, 2019, **48**, 8899–8910.
- 26 R. N. Pradhan, P. Irrera, F. Romdhane, S. K. Panda, D. L. Longo, J. Torres, C. Kremer, A. Assaiya, J. Kumar and A. K. Singh, *Inorg. Chem.*, 2022, **61**, 16650–16663.